A new method to estimate three-dimensional residual mean circulation in the middle atmosphere and its application to gravity-wave resolving general circulation model data

KAORU SATO *, TAKENARI KINOSHITA†

AND KOTA OKAMOTO

Department of Earth and Planetary Science, The University of Tokyo, Tokyo, Japan

J. Atmos. Sci., accepted on 9 August 2013

* *Corresponding author address:* Kaoru Sato, Department of Earth and Planetary Science, The University of Tokyo, Tokyo 113-0033, Japan.

E-mail: kaoru@eps.s.u-tokyo.ac.jp

†Now at National Institute of Information and Communications Technology

ABSTRACT

We propose a new method to estimate three-dimensional (3-d) material circulation driven by waves based on recently-derived formulas by Kinoshita and Sato that are applicable both to Rossby waves and to gravity waves. The residual mean flow is divided into three, i.e., balanced flow, unbalanced flow, and Stokes drift. The latter two are wave-induced components estimated from momentum flux divergence and heat flux divergence, respectively. The unbalanced mean flow is equivalent to the zonal-mean flow in the two-dimensional (2-d) transformed-Eulerian-mean equation (TEM) system. Although these formula were derived using ”time mean”, its underlying assumption is the separation of spatial or temporal scales between the mean and wave fields. Thus, the formulas can be used for both transient and stationary waves. Considering that the average is inherently needed to remove an oscillatory component of unaveraged quadratic functions, the 3-d wave activity flux and wave-induced residual mean flow are estimated by an extended Hilbert transform. In this case, the scale of mean flow corresponds to the whole scale of the wave packet. Using simulation data from a gravity-wave resolving general circulation model, 3-d structure of the residual mean circulation in the stratosphere and mesosphere is examined for January and July. The zonal mean field of estimated 3-d circulation is consistent with the 2-d circulation in the TEM system. An important result is that the residual mean circulation is not zonally-uniform both in the stratosphere and mesosphere. This is likely caused by longitudinally-dependent wave sources and propagation characteristics. The contribution of planetary waves and gravity waves to these residual mean flows is discussed.

1. Introduction

Material circulation of the middle atmosphere is essentially driven by the momentum deposition of atmospheric waves such as gravity waves and Rossby waves propagating from the troposphere as well as the diabatic heating by radiative processes, while differential latent and sensible heatings are also important for the tropospheric circulation. The circulation in the mesosphere forms one cell with a meridional flow from the high latitudes of the summer hemisphere to the high latitudes of the winter hemisphere around the mesopause. The circulation in the stratosphere is mainly composed of two cells from the tropical region to higher latitudes in the two hemispheres and is called the Brewer-Dobson circulation (hereafter referred to as BDC) named after the two scientists who indicated its existence from ozone and water vapor observations. The breaking and/or dissipation of atmospheric waves do not only cause the momentum deposition, but also generate atmospheric turbulence. The geostrophic turbulence associated with Rossby wave breaking is attributable to isentropic irreversible mixing and affects the latitudinal distribution of minor constituents. Thus, it is sometimes considered that the BDC is composed of two elements, i.e., the material circulation driven by the waves and radiative forcing, and the irreversible mixing by the turbulence.

The transformed Eulerian mean (TEM) formulation was introduced by Andrews and McIntyre (1976) to express the two dimensional (2-d) material circulation as the residual mean circulation by taking account of large cancellation between the adiabatic cooling (heating) and the convergence (divergence) of heat flux associated with waves. Dunkerton et al. (1981) showed that the residual mean circulation well approximates Lagrangian mean circulation. Through the adiabatic heating/cooling associated with its vertical flow branch, the residual mean circulation maintains the thermal structure of the middle atmosphere that is far from that expected by radiative balance. The peculiar thermal structure observed in the polar and equatorial regions in the stratosphere and in the polar regions in the mesosphere largely affects the distribution of polar stratospheric clouds in winter and polar mesospheric clouds in summer.

Haynes et al. (1991) proposed the downward control principle using the TEM equations indicating that the zonal-mean stream function at a level is determined by vertical integration of the wave forcing above that level in a steady state. As the equation is linear for the wave forcing, this principle is frequently used to diagnose contribution of respective waves to the driving of the BDC and its trend (e.g., Rosenlof (1995); Butchart et al. (2006); Garcia and Randel (2008); Li et al. (2008); Calvo and Garcia (2009); McLandress and Shepherd (2009); Okamoto et al. (2011); Shepherd and McLandress (2011)). In particular, the amount of tropical upwelling is used as an index of the troposphere-stratosphere mass exchange associated with the BDC. Butchart et al. (2010) compared 11 chemistry-climate model (CCM) simulations for the 21st century in terms of stratospheric climate and circulation. One of the common results from these previous studies using chemistry climate models is that the BDC will have a strengthening trend in response to the climate change of the 21st century. According to Butchart et al. (2010), in most models, orographic gravity waves are of similar importance to the resolved waves both in determining the upwelling and its trend. The annual mean upwelling is attributable to the resolved wave drag by about 67% and to the parameterized orographic gravity wave drag (OGWD) by 30%. The contribution of OGWD to the trend is more important. On average, OGWD explains 59% of the trend in the annal mean upwelling, although the dependence on the model is large. It is considered that the change of the wave forcing is related to upward movement of the breaking region in the upper flanks of the subtropical jets in association with tropospheric warming induced by increasing green house gases (GHG) (Li et al. 2008; McLandress and Shepherd 2009; Okamoto et al. 2011). It is also worth noting that such a change in BDC can affect the characteristics of the quasi-biennial oscillation (Kawatani and Hamilton 2011).

In addition to the strength, the structural change of the BDC has been investigated, especially in terms of the tropical width in the lower stratosphere. Li et al. (2010) examined trend in the latitudinal width of the upward branch of the BDC in the 21st century simulated by a CCM. They showed a narrowing of the upward branch and attributed to the equatorward shift of Rossby waves' critical latitudes under the GHG increase. This is in contrast to the widening trend of the latitudinal region in which the tropical high tropopause is observed over last a few decades as indicated by Seidel and Randel (2007). Seidel and Randel (2007) showed that the tropical widening is associated with the poleward movement of the subtropical jet.

According to the downward control principle, the vertical flow response of the residual mean circulation is observed below and around the latitudinal ends of the wave forcing in a steady state (Haynes et al. 1991). The seasonal cycle may not be treated as a steady state and lead to meridional extension of the circulation away from the forcing region (Holton et al. 1995). Okamoto et al. (2011) used CCM data and estimated the residual mean circulation in December-February directly by its definition and indirectly by using the downward control principle from the Eliassen-Palm flux divergence of resolved waves and parameterized gravity-wave drag. The two different estimates for the residual mean circulation accorded well, suggesting that the steady state assumption is approximately valid even in the seasonal time scales. Moreover, the principle indicates that meridional flow of the residual mean circulation should be maintained by nearby wave forcing. Norton (2006) discussed the importance of equatorial Rossby waves generated by tropical heating in the troposphere for the momentum budget to cause the upwelling in the tropical and subtropical regions. Okamoto et al. (2011) indicated by applying a diagnostic method based on the downward control principle to CCM data and reanalysis data that the summer hemispheric part of the winter circulation in the stratosphere is driven by the subgrid-scale gravity waves. The gravity waves are probably convectively-generated in the summer subtropical region (Sato et al. 2009b). Seviour et al. (2012) examined upward mass flux at 70 hPa using ERA-Interim data for 1989–2009 and showed that the sum of contributions by resolved waves and parameterized orographic gravity waves is 74%, suggesting shortage of orographic and/or non-orographic gravity wave forcing there. On the other hand, Ueyama and Wallace (2010) used temperature data from satellite observation as an index of the vertical flow of the BDC and examined its relation with eddy heat flux in the high latitude region. Their results suggest significant correlation between the high latitude wave forcing and the topical upwelling. They argued that an accumulation of transient responses may explain the broad response in the seasonal time scale. Thus the role of respective kinds of waves in the formation of BDC is still controversial.

Moreover, recent studies show that the BDC is composed of two branches, one is a shallow branch which roughly exhibits hemispheric symmetry in the lowermost stratosphere, and another is a deep branch observed mainly in the winter hemisphere (e.g., Birner and Bönisch (2011)). According to Birner and Bönisch (2011), the transport in the lowermost stratosphere is made by this shallow branch and by isentropic irreversible mixing. The deep branch is slow (time-scale of several months to years) and the shallow branch is fast (time scales of days to a few months). The shallow branch is mainly driven by synoptic-scale waves and partly by gravity waves (Plumb 2002; Miyazaki et al. 2010), while the deep branch is mainly by planetary waves (Plumb 2002) and partly by gravity waves (Okamoto et al. 2011).

So far, the BDC has been examined mainly in the 2-d meridional cross section. However, there are several studies indicating that the BDC has zonally-asymmetric structures. Callaghan and Salby (2002) made a pioneering study to examine three-dimensional (3-d) structure of BDC using an isentropic vertical coordinate. They showed that the cross isentropic flow is not zonally symmetric around a strongly perturbed polar vortex in NH winter. Hitchman and Rogal (2010) indicated the importance of regional outflow of the tropical convection in Southeast Asia for the formation and maintenance of the column ozone maximum situated to the south of Australia. The outflow reinforces the westerly jet by angular momentum transport and subsequently increases synoptic-scale wave activity embedded in the jet. Sato et al. (2009a) showed by using satellite observations that the stratospheric ozone recovery observed in late spring and summer in the Antarctic strongly depends on the longitude. Lin et al. (2009) used data from the satellite-borne Microwave Sounding Unit (MSU) in 1979-2007 and simulation data from a coupled atmosphere-ocean general circulation model (GCM) to examine a horizontal trend pattern of the temperature in SH winter and spring. They showed that the regional dependence of temperature trend is related to those of both column ozone and eddy heat flux. Randel et al. (2010) indicated the importance of an upward flow on the eastern side of the anticyclonic circulation of the Asian monsoon for the transport of hydrogen cyanide (HCN) into the stratosphere. Convection in the Asian and African monsoon regions is also regarded as a strong source of the gravity waves propagating into the upper stratosphere and mesosphere which may drive the zonally-asymmetric BDC (Sato et al. 2009b). These studies suggest that the BDC likely has significant 3-d structure which has not been explored yet.

Recently, Kinoshita and Sato (2013a) derived 3-d transformed Eulerian mean equations including 3-d residual mean flow and 3-d wave activity flux in the primitive equation system. The ”residual mean flow” in the equations was obtained as the sum of the 3-d time mean flow and 3-d Stokes drift associated with waves. Thus, the derived residual mean flow is regarded as an approximation of Lagrangian mean flow. The 3-d wave activity flux was obtained so that its divergence corresponds to the wave forcing of the mean flow in the horizontal momentum equations. This formulation by Kinoshita and Sato (2013a) was made without using any dispersion relations and hence is applicable both to Rossby waves and to gravity waves. In the present study, it is shown that this wave activity flux is written as momentum flux using Lagrangian wind perturbations. Moreover, Kinoshita and Sato (2013b) derived another form of 3-d wave activity flux describing propagation of the wave packet and discussed its relation to the 3-d wave activity flux that appears in the 3-d transformed Eulerian mean equations obtained by Kinoshita and Sato (2013a). The formulation by Kinoshita and Sato (2013b) uses a unified dispersion relation for Rossby waves and gravity waves which was newly derived.

A problem of the formulas by Kinoshita and Sato (2013a,b) is that the time mean is used instead of the zonal mean. Thus, stationary waves cannot be treated, at a glance. However, the formulation by Kinoshita and Sato (2013a,b) is valid if we can assume that the temporal and/or spatial scales of the mean (more precisely speaking, background) field are much longer than those of the perturbation field. In other words, their formulation can be applied for any wave including stationary waves by taking an appropriate mean field. Moreover, taking it into consideration that the average for the flux calculation is inherently needed to remove an oscillatory component of unaveraged quadratic functions on a scale of one-half the wavelength of the wave field, the averaging problem can be overcome by using an extended method of the Hilbert transform which is introduced in the present paper. The extended Hilbert transform is used to estimate the envelop function of momentum or energy fluxes of the wave field as a substitute of the temporal or spatial "mean". The present paper describes a new method to examine the 3-d material circulation using the formulas by Kinoshita and Sato (2013a) and using the extended Hilbert transform. As an example, 3-d structure of the residual mean circulation in the middle and upper stratosphere and mesosphere is examined, utilizing simulation data from a gravity-wave resolving GCM.

A brief description of the high-resolution GCM data used in the present study is given in Section 2. Theoretical consideration of 2-d residual mean circulation and its application to the GCM data are made in Section 3. Some results of the 2-d analysis in Section 3 are not very new but given, because they provide reference materials to lead and validate the theory of 3-d residual mean circulation proposed by the present paper. The 3-d theory is given in Section 4. The treatment of stationary waves in three dimensions using an extended Hilbert transform is also described. Results of the 3-d analysis using the GCM data are shown in Section 5. Summary and concluding remarks are made in Section 6.

2. Short description of gravity-wave resolving GCM data

Utilized data for the analysis are outputs from the T213L256 GCM developed by Watanabe et al. (2008) (the KANTO model), which covers a height region up to 85 km in the upper mesosphere with horizontal resolution of about 60 km and vertical grid spacings of about 300 m above a height of 10 km. No gravity wave parameterizations were included in this model. Thus, all gravity waves are spontaneously generated. The characteristics of simulated gravity waves depend on artificial diffusion and cumulus parameterizations. The set of tuning parameters of the parameterizations was carefully chosen by conducting several sensitivity tests to obtain gravity wave amplitudes in the lower stratosphere which are comparable to radiosonde observations over the central Pacific in the latitudinal range of 28°N to 48°S (Sato et al. 2003). The time integration was made using the Earth Simulator over three model years in which climatology with realistic seasonal variation was specified for the sea surface temperature and stratospheric ozone. Physical quantities were sampled at a short time interval of 1 hour. The model succeeded in simulating zonal mean zonal wind and temperature fields which are consistent with observations, suggesting that the momentum budget including gravity waves is realistic. Watanabe et al. (2008) illustrated an overview of the model performance including the momentum budget. As described by a series of our previous papers using the model data such as Sato et al. (2009b); Kawatani et al. (2010); Sato et al. (2012), overall characteristics of the simulated gravity waves are realistic. The present study examined contribution of gravity waves, synoptic-scale waves and stationary and transient planetary waves to the residual mean circulation. Following our previous studies (Sato et al. 2009b, 2012), small horizontal-scale fluctuations with total wavenumber n $\geq$21 (horizontal wavelengths shorter than 1800 km) are designated as gravity waves (GW). The components with zonal wavenumbers of s=1–3 and s= 4–20 are examined as planetary waves (PW) and synoptic-scale (SW) waves, respectively. Monthly-mean PW component and remaining PW component are analyzed as stationary PW and transient PW, respectively.

3. Two dimensional (2-d) residual mean circulation

a. Theory on the relation between 2-d circulation and E-P flux

The residual mean circulation for 2-d TEM system is composed of two parts: one is ageostrophic wind and the other is Stokes drift. First, it is shown how each part of the residual mean circulation is related to respective terms of Eliassen-Palm (E-P) flux divergence.

By including Coriolis effect, the Lagrangian perturbation of zonal wind u^{L} is expressed as

$$u^{\mathrm{L}} = u' + ([u]_y - f)\eta' + [u]_z\zeta' \equiv u' + u_{(y)} + u_{(z)}, \tag{1}$$

where the square brackets denote the zonal mean, the primes denote the perturbation from the zonal mean, η' and ζ' are latitudinal and vertical displacements, respectively, and f is Coriolis parameter[1]. This formula expresses that u^{L} is the sum of Eulerian zonal wind perturbation u' and

[1]This formula for u^{L} is different from the Lagrangian perturbation u^{l} in Andrews and McIntyre (1976) and Andrews et al. (1987) by an additional term $-f\eta'$

the latitudinal and vertical advection of angular momentum by the perturbation $([u]_y - f)\eta' + [u]_z\zeta'$. Using the following relation[2]

$$[w'\eta'] = -[v'\zeta'] = \frac{[v'\phi'_z]}{N^2}, \tag{2}$$

latitudinal and vertical fluxes of zonal momentum are derived as:

$$\begin{aligned} \rho_0[u^l v'] &= \rho_0([u'v'] + ([u]_y - f)[\eta' v'] + [u]_z[\zeta' v']) & (3)\\ &= \rho_0[u'v'] - \rho_0\frac{[u]_z[v'\phi'_z]}{N^2} & (4)\\ &\equiv Y_1 + Y_2 \end{aligned}$$

and

$$\begin{aligned} \rho_0[u^l w'] &= \rho_0([u'w'] + ([u]_y - f)[\eta' w'] + [u]_z[\zeta' w']) & (5)\\ &= \rho_0[u'w'] + \rho_0\frac{([u]_y - f)[v'\phi'_z]}{N^2} & (6)\\ &\equiv Z_1 + Z_2, \end{aligned}$$

where v and w are latitudinal and vertical wind components, respectively, ϕ is geopotential, ρ_0 is basic state density, and N is the Brunt-Väisälä frequency. Here, the terms $[\eta' v']$ and $[\zeta' w']$ are ignored[3]. Note that suffixes 1 and 2 denote momentum fluxes and heat fluxes, respectively: $Y_1(\equiv \rho_0[u'v'])$ and $Z_1(\equiv \rho_0[u'w'])$ are momentum fluxes and $Y_2(\equiv \rho_0[u_{(z)}v'] = -\rho_0\frac{[u]_z[v'\phi'_z]}{N^2})$ and

[2]The first equality is derived as follows.

$$[w'\eta'] = \mathrm{Re}[WH^*] = \mathrm{Re}[-i\hat{\omega}ZH^*] = -\mathrm{Re}[ZV^*] = -[\zeta' v'],$$

where W, V, H, and Z are "analytic expressions" of w', v', η' and ζ', respectively, and $\hat{\omega}$ is the intrinsic frequency. The "analytic expressions" are described in Section 4 in detail. The second equality is derived from the thermodynamic equation:

$$D\phi'_z/Dt + N^2 w' = D\phi'_z/Dt + N^2(D\zeta'/Dt) = 0,$$

where D/Dt is Lagrangian time derivative. Thus, $\zeta' \approx -\phi_z/N^2$.

[3]Phase difference between $v'(\sim D\eta'/Dt)$ and η' is 90°for the Fourier components having the same wavenumber vector and frequency. Thus $[\eta' v']$ can be ignored. This is also the case for $[\zeta' w']$. Moreover, the covariance of the Fourier components with different wavenumber and/or frequency obviously becomes zero.

$Z_2 (\equiv \rho_0 [u_{(y)} w'] = \rho_0 \frac{([u]_y - f)[v'\phi'_z]}{N^2})$ are proportional to heat fluxes. It is important that (4) and (6) are equivalent to the formulas of y and z components of E-P flux, namely

$$\begin{pmatrix} -F^{EP}_{(y)} \\ \\ -F^{EP}_{(z)} \end{pmatrix} = \begin{pmatrix} \rho_0 [u^l v'] \\ \\ \rho_0 [u^l w'] \end{pmatrix} = \begin{pmatrix} Y_1 \\ \\ Z_1 \end{pmatrix} + \begin{pmatrix} Y_2 \\ \\ Z_2 \end{pmatrix}. \tag{7}$$

Thus, the E-P fux is considered to be the flux of "Lagrangian" zonal momentum. The zonal momentum equation in the 2-d TEM system is

$$[u]_t + ([u]_y - f)[v]^* + [u]_z [w]^* = -\frac{1}{\rho_0}(-\nabla \cdot \boldsymbol{F}^{EP}) + [X], \tag{8}$$

where

$$[v]^* = [v]_{\mathrm{a}} + [v]^{\mathrm{S}} = [v]_{\mathrm{a}} - \frac{1}{\rho_0}\left(\rho_0 \frac{[v'\phi'_z]}{N^2}\right)_z \tag{9}$$

and

$$[w]^* = [w]_{\mathrm{a}} + [w]^{\mathrm{S}} = [w]_{\mathrm{a}} + \left(\frac{[v'\phi'_z]}{N^2}\right)_y, \tag{10}$$

and $[X]$ is the other nonconservative mechanical forcing and friction (e.g. Andrews et al. (1987)).

Comparison between these formulas of residual mean circulation ((9) and (10)) and the divergence of E-P flux (7) indicates that the Stokes drift ($[v]^{\mathrm{S}}$ and $[w]^{\mathrm{S}}$) is related to the divergence of heat fluxes:

$$([u]_y - f)[v]^{\mathrm{S}} + [u]_z [w]^{\mathrm{S}} = -\frac{1}{\rho_0}(Y_{2y} + Z_{2z}). \tag{11}$$

Subtraction of (11) from (8) yields the Eulerian zonal mean zonal momentum equation:

$$[u]_t + ([u]_y - f)[v]_{\mathrm{a}} + [u]_z [w]_{\mathrm{a}} = -\frac{1}{\rho_0}(Y_{1y} + Z_{1z}) + [X]. \tag{12}$$

If it can be assumed that the mean flow is steady and $[X]$ is negligible, this equation indicates that the ageostrophic flow ($[v]_{\mathrm{a}}$ and $[w]_{\mathrm{a}}$) is related to the divergence of momentum fluxes:

$$([u]_y - f)[v]_{\mathrm{a}} + [u]_z [w]_{\mathrm{a}} \approx -\frac{1}{\rho_0}(Y_{1y} + Z_{1z}). \tag{13}$$

Moreover, when $[u]_z$ is small compared with the other terms, the meridional component of ageostrophic flow is approximately written using momentum fluxes as

$$[v]_{\mathrm{a}} \approx \frac{1}{\rho_0}(Y_{1y} + Z_{1z})/\hat{f} = \frac{1}{\hat{f}}\left\{[u'v']_y + \frac{1}{\rho_0}(\rho_0 [u'w'])_z\right\}, \tag{14}$$

where

$$\hat{f} \equiv f - [u]_y. \tag{15}$$

Validity of the assumption of small $[u]_z$ in the middle atmosphere will be discussed in Section 5 using the high-resolution GCM data. This equation indicates that if atmospheric waves with negligibly small heat flux are dominant, the residual mean flow can be estimated only using momentum fluxes. This may be the case for the mesosphere where the gravity wave forcing is dominant. It is worth noting that the estimation of vertical flux of horizontal momentum is possible using Mesosphere-Stratosphere-Troposphere (MST) radar observations, while those of heat flux are generally difficult.

The Stokes drift $[v]^{\mathrm{S}}$ is written using the terms included in the E-P flux similar to $[v]_{\mathrm{a}}$:

$$[v]^{\mathrm{S}} \approx \frac{1}{\rho_0}(Y_{2y} + Z_{2z})/\hat{f}. \tag{16}$$

This equation describes the relation between $[v]^{\mathrm{S}}$ and the terms of the E-P flux, although $[v]^{\mathrm{S}}$ is directly calculated by (9). The important part of the argument in this section is that respective wave contributions to $[v]_{\mathrm{a}}$ are estimated by (14) and those to $[v]^{\mathrm{S}}$ are directly calculated by (9).

b. Results of 2-d analysis using gravity-wave resolving GCM data

Figure 1 shows meridional cross sections of the E-P flux vector $(F^{EP}_{(y)}, F^{EP}_{(z)})$ calculated using (7) by arrows and its divergence by colors for (a) ((e)) all waves, (b) ((f)) PW, (c) ((g)) GW, and (d) ((h)) SW in July (January) of the 2nd model year. Note that GW are resolved waves in the high resolution GCM used in the present study. The distributions in the respective sections for the two months are roughly mirror images of each other.

In the winter mesosphere above about 50 km, the net E-P flux divergence (i.e., contribution by all waves) is negative in most regions of both hemispheres, which is mainly contributed to by GW except the lower part of subtropical westerly region around 60 km. PW also contribute to the negative E-P flux divergence in most latitudes except around 60° depending on the altitude. The positive E-P flux divergence of PW around 60° is related to the generation of eastward 4 day waves (Watanabe et al. (2009), and references therein). Contribution of SW is relatively small but negative in the winter hemisphere except the region around the jet core. In the summer mesosphere, the net E-P flux divergence is positive and mainly explained by the GW contribution and partly by SW and PW contributions. Such dominant GW contribution to the mesospheric momentum budget is consistent with previous theoretical studies (Lindzen 1981; Matsuno 1982; Holton 1982).

In the lower stratosphere of $\sim$15–20 km, the net E-P flux divergence is negative in most latitude regions. Contribution by PW is widely distributed and dominant in the winter middle and high latitudes. Contributions of GW and SW are also large in mid-latitudes of both hemispheres in both months. This significant contribution of GW in this region was also indicated by Miyazaki et al. (2010) and Okamoto et al. (2011).

In the middle and upper stratosphere of $\sim$25–50 km, the net E-P flux divergence is negative in most latitudes of the winter hemisphere and positive in low latitudes of the summer hemisphere. The negative divergence in the winter hemisphere is mainly due to PW, as is consistent with previous studies (see Plumb (2002) and references therein). The positive divergence in the low latitudes of the summer hemisphere is due to GW. This divergence forms the summer hemispheric part of the winter circulation (Okamoto et al. 2011).

An interesting point is that the E-P flux divergence associated with GW is positive in the lower latitude part of the westerly jet in the winter hemisphere. This feature means that the GW accelerate the westerly wind in that region. It is also interesting that there is positive E-P flux divergence around 40 km slightly below the center of the westerly jet in the Southern Hemisphere in July. This positive divergence is due to PW and partly canceled by SW. Similar positive divergence below the westerly jet of the winter hemisphere is observed in some other months (not shown), although it is not evident in January (Fig. 1e). The mechanism causing this positive divergence is interesting, but we leave it for future studies.

Because the purpose of the present study is mainly to demonstrate the usefulness of the new method to examine 3-d material circulation in the atmosphere, further analysis and discussion is focused on the circulation of the middle and upper stratosphere (i.e., the deep branch of BDC) and mesosphere in July and January.

Figure 2a shows the meridional cross section of $[v]^*$ in July that is directly calculated by (9). Figure 2i is also $[v]^*$ but estimated from the divergence of the E-P flux using (14) for $[v]_a$ in (9) under the assumption that the mean wind is steady and the vertical shear of the mean wind is negligible. Overall distributions of $[v]^*$ in Figs. 2a and 2i are similar, assuring the validity of the assumption. Slight difference observed particularly in the summer stratosphere is mainly due to vertical advection of the mean wind by the residual mean flow as shown in Section 5.

The distribution of $[v]_\mathrm{a}$ and $[v]^\mathrm{S}$ are shown in Fig. 2d and Fig. 2g, respectively. In the middle and upper stratosphere ($\sim$25–50 km) except around 40 km, southward flow is dominant in $[v]^*$ which extends from low latitudes of the summer hemisphere to high latitudes of the winter hemisphere (Fig. 2a). This flow is mainly due to $[v]_\mathrm{a}$ in low and middle latitudes of both hemispheres, and due to $[v]^\mathrm{S}$ in high latitudes of the winter hemisphere. The negative $[v]^\mathrm{S}$ in high latitudes of the winter hemisphere is largely canceled by $[v]_\mathrm{a}$, which is consistent with the previous studies (e.g. Dunkerton (1978)).

In the mesosphere, $[v]^*$ extends over the entire latitudes in the winter and summer hemispheres (Fig. 2a). This flow is primarily due to $[v]_\mathrm{a}$ and partly due to $[v]^\mathrm{S}$ in middle latitudes above $\sim$60 km and the whole latitudes below $\sim$60 km in the winter hemisphere. The transition between the stratospheric circulation and mesospheric one is continuous as is also consistent with the schematic view shown by Dunkerton (1978).

Figures 2b and 2c show contribution by PW and GW to $[v]^*$, respectively. Figures 2e, 2f, and 2h show three dominant components of $[v]^*$, namely, $Y_{1y}/\hat{f}$ by PW, $Z_{1z}/\hat{f}$ by GW and $Z_{2z}/\hat{f}$ by PW. It is clear that $[v]_\mathrm{a}$ in the winter hemisphere (Fig. 2d) is comparable to $Y_{1y}/\hat{f}$ by PW below 60 km (Fig. 2e) and $Z_{1z}/\hat{f}$ by GW above (Fig. 2f), while $[v]_\mathrm{a}$ in the summer hemisphere is comparable to $Z_{1z}/\hat{f}$ by GW (Fig. 2f). The Stokes drift $[v]^\mathrm{S}$ (Fig. 2g) is well explained by $Z_{2z}/\hat{f}$ by PW (Fig. 2h) in all latitude and height regions.

From these analyses, it is concluded that the strong southward flow $[v]^*$ in the middle and upper stratosphere (i.e., a deep branch of the BDC) and lower mesosphere below $\sim$60 km is roughly divided into three dominant contributions: $[v]_{\mathrm{a}}$ induced by GW in the summer low latitudes, $[v]_{\mathrm{a}}$ induced by PW in the winter low and middle altitudes, and $[v]^{\mathrm{S}}$ by PW in the winter high latitudes that is partly canceled by the PW-induced $[v]_{\mathrm{a}}$. Moreover, in the middle and upper mesosphere above ∼60 km, $[v]^*$ is mainly contributed to by $[v]_{\mathrm{a}}$ due to GW, and partly by $[v]^{\mathrm{S}}$ due to PW in middle latitudes of the winter hemisphere. It is worth noting here that $[v]^*$ by PW in the mesosphere has interesting structure around 60°S, i.e, positive around 65 km and negative around 50 km. This structure is likely due to 4-day waves generated by in-situ baroclinic/barotropic instability (Watanabe et al. 2009). This fact indicates that the baroclinic/barotropic instability in the winter hemisphere contributes at least partly to the residual mean circulation of the mesosphere.

Figure 3 is the same as Fig. 2 but for the vertical component of the residual mean flow obtained using the continuity equation. Similarity in the distribution in the meridional cross section is also observed between directly-calculated $[w]^*$ (Fig. 3a) and $[w]^*$ estimated from the E-P flux divergence (Fig. 3i).

In the mesosphere, $[w]^*$ is primarily downward in the winter hemisphere, while it is generally upward in the summer hemisphere (Fig. 3a). A characteristic upward flow is also observed in 20°S–50°S in a height region of 50–70 km. These dominant downward and upward residual mean flows are mainly contributed to by GW $Z_{1z}/\hat{f}$. Contribution of PW is relatively weak, but it is upward and downward in higher and lower latitudes than 60°S in the winter hemisphere, respectively. In the equatorial region, a secondary circulation is observed in association with the semiannual oscillation, namely upward (downward) flow in the easterly (westerly) shear region.

In the middle and upper stratosphere, $[w]^*$ is generally downward in the winter hemisphere and upward in the summer hemisphere (Fig. 3a), although $[w]^*$ is weak in middle and high latitudes of the summer hemisphere. The upward flow in the summer hemisphere is mainly due to $Z_{1z}/\hat{f}$ by GW. The downward flow in lower latitudes than about 50°S of the winter hemisphere is due to $Y_{1y}/\hat{f}$ by PW, which is largely canceled by $Z_{2z}/\hat{f}$ of PW and by $Z_{1z}/\hat{f}$ by GW. The downward flow in higher latitudes than about 50°S is mainly due to $Z_{2z}/\hat{f}$ by PW and to $Z_{1z}/\hat{f}$ by GW, which is largely canceled by $Y_{1y}/\hat{f}$ by PW. It is interesting that the contributions by respective waves to $[w]^*$ are different from those to $[v]^*$, although it is understood from the downward control principle. The meridional cross sections of $[v]^*$ and $[w]^*$ and their components in January were roughly mirror images of those in July, although their details are not shown here.

4. Theory of three-dimensional (3-d) residual mean circulation

a. Relation between 3-d residual mean flow and 3-d wave activity flux

Recently Kinoshita and Sato (2013a) derived 3-d transformed Eulerian mean equations including 3-d Stokes drift and 3-d wave activity flux which are applicable both to Rossby waves and gravity waves. The zonal and meridional momentum equations are written as

$$\overline{u}_t + \overline{u}_x\overline{u}^* + (\overline{u}_y - f)\overline{v}^* + \overline{u}_z\overline{w}^* = -\overline{\phi}_x - \frac{1}{\rho_0}(\nabla \cdot \boldsymbol{F}_1) + \overline{X}, \tag{17}$$

$$\overline{v}_t + (\overline{v}_x + f)\overline{u}^* + \overline{v}_y\overline{v}^* + \overline{v}_z\overline{w}^* = -\overline{\phi}_y - \frac{1}{\rho_0}(\nabla \cdot \boldsymbol{F}_2) - f_y\frac{\overline{S_{(p)}}}{f} + \overline{Y}, \tag{18}$$

where

$$\overline{S_{(p)}} \equiv \frac{1}{2}\left(\overline{u'^2} + \overline{v'^2} - \frac{\overline{u'\phi'_y}}{f} + \frac{\overline{v'\phi'_x}}{f}\right), \tag{19}$$

$\boldsymbol{F}_1$ and $\boldsymbol{F}_1$ are the wave activity fluxes as defined below, overbars and primes denote mean and deviation from the mean, $\overline{\boldsymbol{v}}^*(= (\overline{u}^*, \overline{v}^*, \overline{w}^*))$ is the residual mean flow:

$$\overline{\boldsymbol{v}}^* \equiv \overline{\boldsymbol{v}} + \overline{\boldsymbol{v}}^S, \tag{20}$$

and 3-d Stokes drift $\overline{\boldsymbol{v}}^{\mathrm{S}}$ is written as:

$$\overline{u}^{\mathrm{S}} = \overline{(u'\eta')}_y + \frac{1}{\rho_0}(\rho_0\overline{u'\zeta'})_z = \left(\frac{\overline{S_{(p)}}}{f}\right)_y - \frac{1}{\rho_0}\left(\rho_0\frac{\overline{u'\phi'_z}}{N^2}\right)_z, \tag{21}$$

$$\overline{v}^{\mathrm{S}} = -\overline{(u'\eta')}_x + \frac{1}{\rho_0}(\rho_0\overline{v'\zeta'})_z = -\left(\frac{\overline{S_{(p)}}}{f}\right)_x - \frac{1}{\rho_0}\left(\rho_0\frac{\overline{v'\phi'_z}}{N^2}\right)_z, \tag{22}$$

$$\overline{w}^{\mathrm{S}} = -\overline{(u'\zeta')}_x - \overline{(v'\zeta')}_y = \left(\frac{\overline{u'\phi'_z}}{N^2}\right)_x + \left(\frac{\overline{v'\phi'_z}}{N^2}\right)_y. \tag{23}$$

The formulas (21)–(23) are derived without using any dispersion relation. This means that these formulas are applicable both to Rossby waves and to gravity waves.

The wave activity fluxes $\boldsymbol{F}_1 = (F_{11}, F_{12}, F_{13})$ and $\boldsymbol{F}_2 = (F_{21}, F_{22}, F_{23})$ are written as follows.

$$\begin{aligned} F_{11} &= \rho_0 \left(\overline{u'^2} + \frac{\overline{u}_y - f}{f} \overline{S_{(p)}} - \frac{\overline{u}_z}{N^2} \overline{u'\phi'_z} \right) \\ &\equiv X_{11} + X_{12} + X_{13}, \end{aligned} \tag{24}$$

$$\begin{aligned} F_{12} &= \rho_0 \left(\overline{u'v'} - \frac{\overline{u}_x}{f} \overline{S_{(p)}} - \frac{\overline{u}_z}{N^2} \overline{v'\phi'_z} \right) \\ &\equiv Y_{11} + Y_{12} + Y_{13}, \end{aligned} \tag{25}$$

$$\begin{aligned} F_{13} &= \rho_0 \left(\overline{u'w'} + \frac{\overline{u}_x}{N^2} \overline{u'\phi'_z} + \frac{\overline{u}_y - f}{N^2} \overline{v'\phi'_z} \right) \\ &\equiv Z_{11} + Z_{12} + Z_{13}, \end{aligned} \tag{26}$$

$$\begin{aligned} F_{21} &= \rho_0 \left(\overline{u'v'} + \frac{\overline{v}_y}{f} \overline{S_{(p)}} - \frac{\overline{v}_z}{N^2} \overline{u'\phi'_z} \right) \\ &\equiv X_{21} + X_{22} + X_{23}, \end{aligned} \tag{27}$$

$$\begin{aligned} F_{22} &= \rho_0 \left(\overline{v'^2} - \frac{\overline{v}_x + f}{f} \overline{S_{(p)}} - \frac{\overline{v}_z}{N^2} \overline{v'\phi'_z} \right) \\ &\equiv Y_{21} + Y_{22} + Y_{23}, \end{aligned} \tag{28}$$

$$\begin{aligned} F_{23} &= \rho_0 \left(\overline{v'w'} + \frac{\overline{v}_x + f}{N^2} \overline{u'\phi'_z} + \frac{\overline{v}_y}{N^2} \overline{v'\phi'_z} \right) \\ &\equiv Z_{21} + Z_{22} + Z_{23}. \end{aligned} \tag{29}$$

Note that Y_{11}, Y_{13}, Z_{11}, and Z_{13} respectively correspond to Y_1, Y_2, Z_1, and Z_2 in the 2-d TEM equations. It is also worth noting that the residual mean flow $\overline{\boldsymbol{v}}^*$ in (17) and (18) was derived as the sum of mean flow and Stokes drift (21)–(23) in Kinoshita and Sato (2013a), and hence approximately expresses Lagrangian-mean flow. Formulas of the 3-d wave activity flux (24)–(29) were derived as an additional term having forms of the horizontal momentum equations.

Similar to the 2-d theory, it is shown that these fluxes are related to covariance of Lagrangian wind perturbations (u^{L} and v^{L}) and wind fluctuations ($\boldsymbol{v}' \equiv (u', v', w')$)

$$\boldsymbol{F}_1 = \rho_0 \overline{u^{\mathrm{L}} \boldsymbol{v}'}, \tag{30}$$

$$\boldsymbol{F}_2 = \rho_0 \overline{v^{\mathrm{L}} \boldsymbol{v}'}, \tag{31}$$

where

$$u^{\mathrm{L}} \equiv u' + \overline{u}_x \xi' + (\overline{u}_y - f)\eta' + \overline{u}_z \zeta' \equiv u' + u_{(x)} + u_{(y)} + u_{(z)}, \tag{32}$$

$$v^{\mathrm{L}} \equiv v' + (\overline{v}_x + f)\xi' + \overline{v}_y \eta' + \overline{v}_z \zeta' \equiv v' + v_{(x)} + v_{(y)} + v_{(z)}. \tag{33}$$

This point is not explicitly described in Kinoshita and Sato (2013a).

Here it should be emphasized that these 3-d TEM equations are derived only assuming that the temporal or spatial scales of the mean and perturbation fields are separable, although Kinoshita and Sato (2013a) supposed time mean. More specifically speaking, the mean field is slow (large-scale) field, and the perturbation field is fast (small-scale) field, when we consider temporal (spatial) scales. Thus the 3-d momentum equations (17) and (18) include time and spatial derivatives for mean-field scales. See Kinoshita and Sato (2013a) for details of the derivation. In summary, the derived 3-d formulas hold for any mean if the mean field is distinguished from the perturbation field by their scales. This point is important to estimate the contribution of stationary waves to the residual mean flow as discussed later.

The residual mean flow $\overline{\boldsymbol{v}}^*$ is composed of three terms:

$$\overline{\boldsymbol{v}}^* = \overline{\boldsymbol{v}}_{\mathrm{b}} + \overline{\boldsymbol{v}}_{\mathrm{a}} + \overline{\boldsymbol{v}}^{\mathrm{S}}, \tag{34}$$

where $\overline{\boldsymbol{v}}_{\mathrm{b}}$ ($= (\overline{u}_{\mathrm{b}}, \overline{v}_{\mathrm{b}}, 0)$) is balanced mean flow (such a flow that satisfies a balance of forces including pressure gradient force), $\overline{\boldsymbol{v}}_{\mathrm{a}}$ ($= (\overline{u}_{\mathrm{a}}, \overline{v}_{\mathrm{a}}, \overline{w}_{\mathrm{a}})$) is unbalanced mean flow, and $\overline{\boldsymbol{v}}^{\mathrm{S}}$ ($= (\overline{u}^{\mathrm{S}}, \overline{v}^{\mathrm{S}}, \overline{w}^{\mathrm{S}})$) is Stokes drift.

A simplest balanced mean flow is the geostrophic flow:

$$-f\overline{v}_g = -\overline{\phi}_x, \tag{35}$$

$$f\overline{u}_g = -\overline{\phi}_y. \tag{36}$$

For strong flow, we may need to consider the gradient wind balance (see Randel (1987)).

The unbalanced mean flow is defined as the departure of the mean flow $\overline{\boldsymbol{v}}$ from the balanced mean flow.

$$\overline{\boldsymbol{v}}_{\mathrm{a}} \equiv \overline{\boldsymbol{v}} - \overline{\boldsymbol{v}}_{\mathrm{b}}. \tag{37}$$

The unbalanced mean flow $\overline{\boldsymbol{v}}_{\mathrm{a}}$ is equivalent to the ageostrophic flow $[\boldsymbol{v}]_{\mathrm{a}}$ in 2-d TEM equations.

Similar to the 2-d theory discussed in Section 3, respective correspondences can be considered between $\overline{\boldsymbol{v}}^*$ and the divergence of the 3-d wave activity flux. First, it is seen from comparison between (21)–(23) and (24)–(29) that the sum of the mean flow advection by Stokes drift and Coriolis acceleration associated with Stokes drift exactly equals to the divergences of heat flux and $\overline{S_{(p)}}$ in the following.

$$\overline{u}_x\overline{u}^{\mathrm{S}} + (\overline{u}_y - f)\overline{v}^{\mathrm{S}} + \overline{u}_z\overline{w}^{\mathrm{S}} = -\frac{1}{\rho_0}(X_{12x} + X_{13x} + Y_{12y} + Y_{13y} + Z_{12z} + Z_{13z}), \tag{38}$$

$$(\overline{v}_x + f)\overline{u}^{\mathrm{S}} + \overline{v}_y\overline{v}^{\mathrm{S}} + \overline{v}_z\overline{w}^{\mathrm{S}} = -\frac{1}{\rho_0}(X_{22x} + X_{23x} + Y_{22y} + Y_{23y} + Z_{22z} + Z_{23z}) + \frac{f_y}{f}\overline{S_{(p)}}. \tag{39}$$

These equations are those to be compared to (11) in the 2-d TEM system.

The relation between the unbalanced mean flow and 3-d wave activity flux divergence is not so simple as for the 2-d theory, but depends on the definition of the balanced flow. However, by analogy with the 2-d theory, the unbalanced mean flow induced by the wave forcing is defined so as to satisfy the following relation when the mean flow is approximately steady and $\overline{X}$ and $\overline{Y}$ are negligible :

$$\overline{u}_x\overline{u}_{\mathrm{a}} + (\overline{u}_y - f)\overline{v}_{\mathrm{a}} + \overline{u}_z\overline{w}_{\mathrm{a}} \approx -\frac{1}{\rho_0}(X_{11x} + Y_{11y} + Z_{11z}), \tag{40}$$

$$(\overline{v}_x + f)\overline{u}_{\mathrm{a}} + \overline{v}_y\overline{v}_{\mathrm{a}} + \overline{v}_z\overline{w}_{\mathrm{a}} \approx -\frac{1}{\rho_0}(X_{21x} + Y_{21y} + Z_{21z}). \tag{41}$$

If we can assume that the terms proportional to $\overline{u}_x$, $\overline{u}_z$, $\overline{v}_x$, $\overline{v}_y$, $\overline{v}_z$ and f_y are small, the 3-d unbalanced mean flow is approximately obtained from the wave activity flux:

$$\overline{u}_{\mathrm{a}} \approx -\frac{1}{\rho_0}(X_{21x} + Y_{21y} + Z_{21z})/f = -\frac{1}{f}\left[(\overline{u'v'})_x + (\overline{v'^2})_y + \frac{1}{\rho_0}(\rho_0\overline{v'w'})_z\right], \tag{42}$$

$$\overline{v}_{\mathrm{a}} \approx \frac{1}{\rho_0}(X_{11x} + Y_{11y} + Z_{11z})/\tilde{f} = \frac{1}{\tilde{f}}\left[(\overline{u'^2})_x + (\overline{u'v'})_y + \frac{1}{\rho_0}(\rho_0\overline{u'w'})_z\right], \tag{43}$$

where

$$\tilde{f} \equiv f - \overline{u}_y. \tag{44}$$

The vertical wind component of the unbalanced mean flow $\overline{w}_{\mathrm{a}}$ is estimated by the continuity equation:

$$\overline{u}_{ax} + \overline{v}_{ay} + \frac{1}{\rho_0}(\rho_0\overline{w}_{az}) = 0. \tag{45}$$

The validity of the definition of $\overline{\boldsymbol{v}}_{\mathrm{a}}$ and the assumptions in (42) and (43) can be confirmed by accordance of the zonal mean of estimated 3-d flows with the directly-calculated zonal mean 2-d flows using the data as will be made in Section 5. An important point is that the terms on the right of (21)–(23) and (42)–(43) are written with the wave fluxes only. This means that the contributions of respective waves to the 3-d residual mean flows are separately estimated. Hereafter, the wave contribution to the residual mean flow, i.e., the sum of $\overline{\boldsymbol{v}}^{\mathrm{S}}$ and $\overline{\boldsymbol{v}}_{\mathrm{a}}$ is referred to as unbalanced residual mean flow $\overline{\boldsymbol{v}}^{\dagger}$:

$$\overline{\boldsymbol{v}}^{\dagger} \equiv \overline{\boldsymbol{v}}^{\mathrm{S}} + \overline{\boldsymbol{v}}_{\mathrm{a}}. \tag{46}$$

Last but not least, it should be emphasized that there is a role of zonally-symmetric fluctuations in the 3-d TEM system, although it is treated as the mean field in the 2-d TEM system. For example, gravity waves with horizontal wavenumber vectors pointing meridionally have zonally-symmetric but meridionally fluctuating structure. Such gravity waves have significant values of $\overline{v'^2}$, $\overline{v'w'}$ and $\overline{u'\phi'_z}$. The divergence of these wave fluxes appears in the mean meridional momentum equation (18) and can cause $\overline{u}^{\dagger}$. Several previous studies (e.g., Lieberman (1999); Miyahara et al. (2000)) suggested the importance of such wave activity flux divergence in the meridional momentum equation in the mesosphere and lower thermosphere.

b. *Treatment of stationary waves in 3-d analysis using an extended Hilbert transform*

As already mentioned, when the time mean is used for an average, the 3-d residual mean circulation and wave activity flux cannot be calculated for stationary waves. However, the average is inherently needed for smoothing out an oscillatory component of unaveraged quadratic functions. We propose therefore to use an extended Hilbert transform, which is newly introduced in the present study, for the smoothing.

Hilbert transform is a procedure to obtain an envelop function of a particular wave packet. We extend this procedure to obtain the wave activity flux and Stokes drift whose temporal and/or spatial structure is comparable to the whole scale of the wave packet. In other words, the scale of the ”mean” field is taken as that of the background field which the ”wave packet” interacts with.

The Hilbert transform $H[a(t)]$ of a particular time series $a(t)$ is the time series that is composed of Fourier components of $a(t)$ whose phases are shifted by $-\pi/2$ radians, namely,

$$a(t) = \sum_{\omega} A_{\omega} \sin(\omega t + \varphi_{\omega}), \tag{47}$$

$$H[a(t)] = -\sum_{\omega} A_{\omega} \cos(\omega t + \varphi_{\omega}), \tag{48}$$

where ω is the ground-based frequency and φ_{ω} is an arbitrary phase (e.g., Bracewell (1999)).

An extended Hilbert transform $H[a(\boldsymbol{x}, t)]$, hereafter referred to as e-HT, of a particular fluctuation field $a(\boldsymbol{x}, t)$ is defined as an arbitrary fluctuation field composed of Fourier components of $a(\boldsymbol{x}, t)$ whose phases are shifted by $-\pi/2$ radians:

$$a(\boldsymbol{x}, t) = \sum_{\boldsymbol{k},\omega} A_{\boldsymbol{k},\omega} \sin(\boldsymbol{k} \cdot \boldsymbol{x} - \omega t + \varphi_{\boldsymbol{k},\omega}), \tag{49}$$

$$H[a(\boldsymbol{x}, t)] = -\sum_{\boldsymbol{k},\omega} A_{\boldsymbol{k},\omega} \cos(\boldsymbol{k} \cdot \boldsymbol{x} - \omega t + \varphi_{\boldsymbol{k},\omega}), \tag{50}$$

where $\boldsymbol{k} \equiv (k, l, m)$ is a wavenumber vector and k, l, m are zonal, meridional and vertical wavenumbers, respectively, and $\varphi_{\boldsymbol{k},\omega}$ is an arbitrary phase. An analytic representation of the real function $a(\boldsymbol{x}, t)$ is defined as a complex function $A(\boldsymbol{x}, t)$ ($\equiv a(\boldsymbol{x}, t) + iH[a(\boldsymbol{x}, t)]$). The envelop function $A_{\text{env}}(\boldsymbol{x}, t)$ of $a(\boldsymbol{x}, t)$ is obtained by using $A(\boldsymbol{x}, t)$.

$$\frac{1}{2} A_{\text{env}}(\boldsymbol{x}, t)^2 = \frac{1}{2} A(\boldsymbol{x}, t) A^*(\boldsymbol{x}, t), \tag{51}$$

where $A^*(\boldsymbol{x}, t)$ denotes the complex conjugate of $A(\boldsymbol{x}, t)$. This corresponds to an average of $a(\boldsymbol{x}, t)^2$:

$$< a(\boldsymbol{x}, t)^2 >= \frac{1}{2} A(\boldsymbol{x}, t) A^*(\boldsymbol{x}, t), \tag{52}$$

where angle brackets $<>$ mean an average with a scale expressing the overall structure of wave packet. Similarly, flux quadratics $< a(\boldsymbol{x}, t) b(\boldsymbol{x}, t) >$ are obtained as

$$< a(\boldsymbol{x}, t) b(\boldsymbol{x}, t) >= \frac{1}{2} \mathrm{Re}[A(\boldsymbol{x}, t) B^*(\boldsymbol{x}, t)]. \tag{53}$$

Note again that in this method, the envelop scale is roughly regarded as that of the background field which the wave packet interacts with.

Examples of the estimation of the envelop function using the e-HT are illustrated in Fig. 4. Figure 4a shows a fluctuation field of a particular quantity forming two wave packets. Figures 4b and 4c show the results of the envelop function estimation by applying the e-HT in x and y directions, respectively. It is clear that the envelop function of the wave packet is successfully obtained with the e-HT in the x direction, while this is not the case for the estimate with the e-HT in the y direction. The failure of the estimate in the y direction is attributable to too small number of the wave crests (less than 1) in that direction. In other words, the wave packets cannot be distinguished from the background field in the y direction. Thus, the e-HT should be made in such a direction that the waves can be distinguished from the mean field. For example, quasi-stationary waves are hardly distinguished from the time mean field, but can be distinguished from the zonal mean field. Thus, quasi-stationary waves are extracted as deviation from the zonal mean, and the e-HT should be applied in the zonal direction. In general, the e-HT should be taken in time or spatial direction in which the waves are fluctuating. When waves are fluctuating in more than two directions, the envelop function can be estimated taking the e-HT in only one of the directions, because what we need is to make phase shift by $-\pi/2$ radians.

Figure 4d illustrates an example of application of the e-HT to stationary waves. The solid red curve shows a longitudinal profile of a particular quantity $a(x)$ that is composed of $s = 1, 2, 3$ components (red dashed curves). The extended Hilbert transform of $a(x)$ ($H[a(x)]$) in the x direction is shown by the blue curve. The envelop function $A_{\text{env}}(x)$ is obtained using (52) as denoted by the thick black curve. It is clear that $A_{\text{env}}(x)$ describes the longitudinal structure of the planetary wave ”packet”.

It is important that the e-HT can be obtained also for transient waves. Therefore, using the e-HT, it is possible to estimate the wave activity flux and the 3-d residual mean flow using (53) for any wave packet. In the present study, this method using the e-HT is applied to estimate the residual mean flows associated with GW and PW including both stationary and transient components.

5. Results of the 3-d analysis using gravity-wave resolving GCM data

As seen from the results of the 2-d analysis in Section 3, dominant waves contributing to the residual mean flow in the middle atmosphere are PW and GW. Thus, in this section, we examine contributions of three kinds of wave fields, namely, ”all” waves defined as the departure from the zonal mean, PW having s=1–3 and GW having $n \geq 21$ using the derived formulas. Moreover, a monthly-mean PW field and the deviation from the monthly-mean are analyzed as stationary and transient PW components, respectively. These definitions of PW and GW are the same as for the 2-d analysis. Monthly-mean zonal-mean zonal wind and Brunt-Väisälä frequency are used as $\overline{u}$ and N for the wave flux calculation. This way to take the mean fields may not be appropriate for the estimation for GW when PW having large amplitudes are present. In a such case, $\overline{u}_y$ should be defined locally. However, in the case of the present study, the difference between the estimates using zonal mean $\overline{u}_y$ and locally defined $\overline{u}_y$ was quite small (not shown). The unbalanced residual mean flow $\overline{\boldsymbol{v}}^{\dagger}$ in the 3-d space was obtained using the e-HT (53) by a phase shift in the x direction for the three kinds of wave fields at each time. The Stokes drift $\overline{\boldsymbol{v}}^{\mathrm{S}}$ was obtained using (21)–(23), and the unbalanced mean flow $\overline{\boldsymbol{v}}_{\mathrm{a}}$ was estimated using (42), (43), and (45). Furthermore, $\overline{\boldsymbol{v}}^{\mathrm{S}}$ and $\overline{\boldsymbol{v}}_{\mathrm{a}}$ obtained for respective wave fields were averaged over a month to examine the residual mean flow for each month.

First, in order to confirm the validity of the 3-d analysis method, consistency with the result of the 2-d TEM analysis is examined. The most strict comparison may be for the unbalanced mean flow because the formulas were derived under the largest number of assumptions for the mean wind unlike Stokes drift. Figures 5a and 5b show the meridional cross sections of the zonal mean $\overline{v}_{\mathrm{a}}$ and $[v]_{\mathrm{a}}$ that are estimated from the momentum fluxes associated with all waves using (43) and (14), respectively. Note that the flow in Fig. 5a includes contribution of stationary waves that is estimated using the e-HT.

It is important that the zonal mean $\overline{v}_{\mathrm{a}}$ (Fig. 5a) and $[v]_{\mathrm{a}}$ (Fig. 5b) agree quite well in terms of the distribution and magnitude, although they are not exactly the same. Moreover, the distributions of the unbalanced mean meridional flow shown in Figs. 5a and 5b accord well with the meridional cross section of $[v]_{\mathrm{a}}$ that was directly estimated (Fig. 2d), indicating that underlying assumptions for the mean wind are approximately valid. The slight difference is observed in the lower part of easterly jet in the summer hemisphere. This mainly comes from the vertical advection of the mean wind $w_{\mathrm{a}}[u]_z/\hat{f}$ (Fig. 5d). The mean zonal wind tendency term $[u]_t/\hat{f}$ is not significant (Fig. 5e). Figure 5c shows the meridional cross section of estimated $[v]_{\mathrm{a}}$ including the correction term of $w_{\mathrm{a}}[u]_z/\hat{f}$ (see equation (13)). The agreement becomes better. These results support that the method to estimate 3-d unbalanced mean flow from momentum flux divergence is appropriate. Note that the zonal mean of $\overline{v}^{\mathrm{S}}$ is exactly and analytically equal to $[v]^{\mathrm{S}}$, if the wave fluxes for the same wave components are taken into account (see (9) and (22)).

a. The 3-d unbalanced residual mean flow and contribution by PW and GW at 10 hPa in July

The maps of the meridional components of the residual mean flow induced by waves $\overline{v}^{\dagger}$, unbalanced mean flow $\overline{v}_{\mathrm{a}}$ and Stokes drift $\overline{v}^{\mathrm{S}}$ at 10 hPa ($\sim$32 km) for all waves, PW, and GW are shown in Fig. 6 for July of the 2nd model year. Note that the color scale is different for the maps for GW from those for all waves and PW. The flows shown in Fig. 6 include the contribution of stationary waves estimated using the e-HT. The most important feature is that these flows, and hence the Brewer-Dobson circulation, are not zonally uniform.

In the NH, negative $\overline{v}^{\dagger}$ for all waves (Fig. 6a) is dominant in the Indian and African monsoon regions and mainly contributed to by $\overline{v}_\mathrm{a}$ due to GW (Fig. 6f). It is also interesting that weak positive $\overline{v}^\dagger$ is observed in SH low latitudes for GW. This is due to the eastward GW force as already indicated in Section 3b. It is worth noting here that weak $\overline{v}^\mathrm{S}$ by GW is consistent with theoretical characteristics of linear inertia-gravity waves: the momentum fluxes (Z_{11}) are larger than heat fluxes (Z_{13}) (e.g., Sato et al. (1997)).

Another interesting feature observed in $\overline{v}^\dagger$ by GW is significantly negative and positive values to the west and east of the Southern Andes, respectively. This is explained by the fact that zonal wind variances associated with topographically-forced GW are confined over the mountains, although a part of GW energy propagates leeward by the mean wind perpendicular to the wavenumber vector (e.g., Preusse et al. (2002), Sato et al. (2012)). This feature is also indicated by Kinoshita and Sato (2013a).

In SH, the three kinds of flows $\overline{v}^\dagger$, $\overline{v}_\mathrm{a}$, and $\overline{v}^\mathrm{S}$ by all waves are dominated by PW. Unbalanced mean flow $\overline{v}_\mathrm{a}$ is mainly observed in the Western Hemisphere. It is negative in lower latitudes than about 40°S and positive in higher latitudes. On the other hand, negative $\overline{v}^\mathrm{S}$ is longitudinally widely distributed. The positive $\overline{v}_\mathrm{a}$ is canceled by the negative $\overline{v}^\mathrm{S}$ in the higher latitudes of the Western Hemisphere. However, because the dominant regions of positive $\overline{v}_\mathrm{a}$ and negative $\overline{v}^\mathrm{S}$ are slightly different, weak equatorward $\overline{v}^\dagger$ is observed in a part of the Western Hemisphere even in the winter hemisphere. The residual mean flow $\overline{v}^\dagger$ by waves in the Eastern Hemisphere is negative and mainly explained by $\overline{v}^\mathrm{S}$.

b. Contribution of stationary and transient waves in three dimensions in July

Further examination was made by dividing PW into stationary and transient wave components. The results of the 3-d analysis for 10 hPa are shown in Fig. 7. It is clear that the dominant $\overline{v}_\mathrm{a}$ in the SH western longitudes seen in Fig. 6e is mainly explained by stationary PW. The Stokes drift $\overline{v}^\mathrm{S}$ by stationary PW is also dominant in the Western Hemisphere. Contours in Fig. 7 show time mean geopotential height. The meandering contours indicate that the amplitude of stationary PW is certainly large in the Western Hemisphere. On the other hand, the distribution of $\overline{v}_\mathrm{a}$ and $\overline{v}^\mathrm{S}$ by transient PW is more zonally uniform compared with that by stationary PW.

c. The 3-d unbalanced residual mean flow at 10 hPa in January

Figure 8 shows $\overline{v}^{\dagger}$ by all waves, by PW and by GW in January of the 2nd model year at 10 hPa. The unbalanced meridional mean flow is again not zonally uniform. Strong northward flow in NH is observed over the Pacific and in America in low and middle latitudes, and in Eurasia in middle and high latitudes. This flow is mainly due to PW, although the distributions of $\overline{v}^{\dagger}$ by all waves and that by PW do not accord so well as those for in July. GW contribution to $\overline{v}^{\dagger}$ in NH is small but has negative values in the Western Pacific and East America to the Western Atlantic in middle latitudes. These regions correspond to storm tracks. Thus, GW contributing to the negative $\overline{v}^{\dagger}$ likely originate from jet-front systems. In SH, there is systematic northward flow by GW in low latitudes, although total $\overline{v}^{\dagger}$ is weak. Roughly speaking, the longitudinal distribution is uniform, but values are slightly enhanced to the east of continents, i.e., Africa, Australia and South America. This suggests a possible role of GW which are generated by convection associated with the monsoon in these regions.

d. The 3-d unbalanced residual mean flow at 0.05 hPa in July and January

Results of the 3-d analysis in the mesosphere is shown in Fig. 9 for $\overline{v}^{\dagger}$ by all waves, by PW and by GW in July and January of the 2nd model year at 0.05 hPa ($\sim$70km). Note that color scales are the same for all maps for all waves, PW and GW unlike the maps at 10 hPa. In July (January), $\overline{v}^{\dagger}$ generally southward (northward) in the entire region at this level. It is clear that GW contribution is dominant, although PW contribution is also large in low latitudes of the winter hemisphere in both months.

The distribution of $\overline{v}^{\dagger}$ is not zonally uniform. In the summer hemisphere, $\overline{v}^{\dagger}$ due to GW is large in several subtropical regions, i.e., 80°E–160°E and 80°W–60°W in NH in July and 20°E–80°E, 140°E–150°W, and 60°W–10°W in SH in January. On the other hand, the mean wind is primarily zonally uniform as seen from zonally-elongated geopotential contours in Fig. 9. This feature is common for the stratosphere and lower mesosphere (not shown). This is because planetary waves originating from the troposphere hardly propagate into the easterly wind in the middle atmosphere in summer (the Charney-Drazin theorem, see Andrews et al. (1987)). Thus, it is likely that the longitudinal variation of $\overline{v}^{\dagger}$ is reflected by GW sources. In fact, these strong $\overline{v}^{\dagger}$ regions are located to the east of monsoon region. The longitudinal difference between the dominant regions of $\overline{v}^{\dagger}$ by GW and the monsoon regions at 0.05 hPa is larger than that at 10 hPa, suggesting eastward propagation of the GW packets from the source. In the winter hemisphere, the distribution of $\overline{v}^{\dagger}$ is complicated. Vertical filtering of GW in the background field that is modified by larger-scale waves and non-zonal GW source distribution are likely mechanisms (Smith 2003; Sato et al. 2009b).

Such non-zonal distribution of $\overline{v}^{\dagger}$ by GW drag may be a source of PW which has large amplitudes in the upper mesosphere and lower thermosphere (Smith 2003). It is worth noting here again that $\overline{v}^{\dagger}$ by PW is at least partly related to baroclinic/barotropic instability in which unstable fields are formed by GW forcing (Watanabe et al. (2009) and references therein). The results of the 3-d analysis in the present study suggest the possibility that the phase structure of PW generated by the instability is determined by the longitudinal distribution of GW drag. This is an interesting issue for future studies.

Although the results were mainly shown for July and January of the 2nd year so far, we also examined the data in July of the 1st and 3rd years. The results are generally consistent with those of the 2nd year. Notable differences between the three years are dominant longitudes of stationary PW and the strength of the flows in the monsoon regions induced by GW. However, these are probably explained by interannual variability of the atmospheric circulation.

e. The 3-d residual mean flow in the polar stereographic map

In this subsection, we show the polar stereographic maps of 3-d residual mean flow vector $\overline{\boldsymbol{v}}^{\dagger}$ ($\equiv \overline{\boldsymbol{v}}_{\mathrm{a}} + \overline{\boldsymbol{v}}^{\mathrm{S}}$) induced by waves where $\overline{\boldsymbol{v}}_{\mathrm{a}}$ is estimated using (42), (43) and (45), and $\overline{\boldsymbol{v}}^{\mathrm{S}}$ is calculated using (21)–(23).

Results are shown for 10 hPa in SH in July of the 2nd year in Fig. 10. The horizontal wind components ($\overline{u}^{\dagger}$ and $\overline{v}^{\dagger}$) in Fig. 10a tend to westward in low latitudes and eastward in high latitudes. However, they are not zonally uniform. The westward flow in low latitudes and eastward flow in high latitudes are confluent to the south of Australia and merged into the eastward flow around the polar night jet. The westward flow in low latitudes is mainly due to unbalanced mean flow, and eastward flow is a mixture of unbalanced mean flow and Stokes drift (Figs. 10c and 10e).

The vertical wind component $\overline{w}^{\dagger}$ is relatively complicated as shown in Fig. 10b. Strong downward flow is observed in longitudes clockwise from 60°W to 60°E along the polar night jet. In the remaining longitude region including the date line, strong downward flow extends toward lower latitudes ($\sim$30°S), although downward flow is also observed inside the polar vortex. These downward flows are mainly due to unbalanced mean flow $\overline{w}_{\mathrm{a}}$. The Stokes drift $\overline{w}^{\mathrm{S}}$ is strong except for the longitude region clockwise from 60°E to 120°E, and it is downward (upward) inside (outside) the polar vortex. The downward $\overline{w}^{\mathrm{S}}$ inside the polar vortex is largely canceled by upward $\overline{w}_{\mathrm{a}}$.

Figure 11 shows contributions of PW and GW to $\overline{\boldsymbol{v}}^{\dagger}$. Note that color scale and unit vector are different for GW from those in Fig. 10 while those for PW are the same. Comparing with Fig. 10, it is seen that overall structure is mainly determined by the residual mean flow induced by PW forcing. However, it is worth noting that characteristic downward and upward flows are observed around the Southern Andean region, which is likely associated with topographically-forced GW.

Next, polar stereographic maps of 3-d residual mean flow at 10 hPa in NH in July of the 2nd year and those in SH and NH in January of the 2nd year are shown in Fig. 12. In both summer hemispheres, horizontal components of $\overline{\boldsymbol{v}}^{\dagger}$ is large only in subtropical regions (Figs. 12a and 12c). The upward flow $\overline{w}^{\dagger}$ is strong in the Asian and African monsoon region in NH in July, while longitudinal variation of $\overline{w}^{\dagger}$ is not large in SH in January (Figs. 12b and 12d). The strong upward flow in the NH monsoon region is consistent with the previous study by Randel et al. (2010) who examined the upward transport of minor constituents using a satellite observation and CCM simulation.

On the other hand, $\overline{\boldsymbol{v}}^{\dagger}$ in NH in January has interesting structure. The zonal component $\overline{u}^{\dagger}$

tends to be westward in low latitudes and eastward in high latitudes as is similar to that in SH in July (Fig. 12e). Strong downward flow is observed in two longitudinal regions clockwise from 30°W to 120°W and from 170°E to 50°E around the polar night jet. The strong downward flows around the jet extend to lower latitudes having a spiral-like form. It is also interesting that upward flow is observed even in NH in this month (i.e., winter).

Last, polar stereographic maps of $\overline{\boldsymbol{v}}^{\dagger}$ at 0.05 hPa in the mesosphere are shown (Fig. 13). In the winter hemisphere (Figs. 13a, 13b, 13g, and 13h), the polar vortex is larger than that at 10 hPa. The horizontal component $\overline{\boldsymbol{v}}^{\dagger}$ is generally eastward and poleward around the westerly jet. The downward flow area is spread toward 120°W in SH in July, while it is confined to high latitudes in the Western Hemisphere in NH in January. Moreover, a strong downward flow is observed around the Southern Andes and Antarctic Peninsula in Fig. 13b in SH in July, which is likely due to gravity waves forced topographically in that region. It is important that the distributions of $\overline{w}^{\dagger}$ observed in Figs. 13b and 13h have some similarity to those at 10 hPa in Figs. 10b and 12f, respectively. This fact can be explained by the downward control principle indicating that the vertical flow in the stratosphere is largely affected by wave forcing in the mesosphere and above.

In the summer hemisphere shown in Figs. 13c, 13d, 13e, and 13f, the distribution of $\overline{\boldsymbol{v}}^{\dagger}$ is relatively zonally uniform compared with that in the winter hemisphere. The zonal component $\overline{u}^{\dagger}$ is large and generally eastward in the subtropical region. There is slight hemispheric difference in the distribution of upward motion: The upward motion is stronger and distributed in higher latitudes in NH than in SH. The distribution can be affected by the location and strength of the (simulated) easterly jet which modify lateral propagation of GW (Sato et al. 2009b). Further detailed discussion is beyond the scope of the present paper, however.

f. Comparison with 3-d time-mean flow

As we mentioned in Section 4, the residual mean flow $\overline{\boldsymbol{v}}^{*}$ is the sum of balanced mean flow $\overline{\boldsymbol{v}}_{\mathrm{b}}$ and unbalanced residual mean flow $\overline{\boldsymbol{v}}^{\dagger}$ ($\equiv \overline{\boldsymbol{v}}_{\mathrm{a}} + \overline{\boldsymbol{v}}^{\mathrm{S}}$). In order to see the relative strength of $\overline{\boldsymbol{v}}_{\mathrm{b}}$ and $\overline{\boldsymbol{v}}^{\dagger}$, the time mean flow $\overline{\boldsymbol{v}}$ ($= \overline{\boldsymbol{v}}_{\mathrm{b}} + \overline{\boldsymbol{v}}_{\mathrm{a}}$) is calculated. Results are shown in Fig. 14. Note that the color scales for $\overline{\boldsymbol{v}}$ and for $\overline{\boldsymbol{v}}^{\dagger}$ are different for 10 hPa, and are the same for 0.05 hPa.

At 10 hPa, the magnitude of $\overline{\boldsymbol{v}}$ is much larger than that of $\overline{\boldsymbol{v}}^{\dagger}$ in the winter hemisphere. This is the case for the summer hemisphere, although $\overline{\boldsymbol{v}}$ is not visible with this color scale. This result indicates that $\overline{\boldsymbol{v}}_{\mathrm{b}}$ is dominant in $\overline{\boldsymbol{v}}^{*}$ by its magnitude. However, it should be emphasized that $\overline{\boldsymbol{v}}_{\mathrm{b}}$ does not contribute to the zonal mean mass transport in the meridional cross section.

On the other hand, the magnitude of $\overline{\boldsymbol{v}}$ is comparable to that of $\overline{\boldsymbol{v}}^{\dagger}$ at 0.05 hPa. However, the distribution of $\overline{\boldsymbol{v}}$ is largely different from $\overline{\boldsymbol{v}}^{\dagger}$ in the winter hemisphere. The planetary-scale pattern with positive and negative values is observed in $\overline{\boldsymbol{v}}$, reflecting the existence of large amplitude PW. In the summer hemisphere, $\overline{\boldsymbol{v}}$ is similar to $\overline{\boldsymbol{v}}^{\dagger}$ both in the magnitude and distribution. This means that in the summer hemisphere, $\overline{\boldsymbol{v}}_{\mathrm{b}}$ is small, and $\overline{\boldsymbol{v}}^{*}$ is primarily determined by $\overline{\boldsymbol{v}}_{\mathrm{a}}$ which is mainly due to GW.

6. Summary and concluding remarks

A new method to estimate three-dimensional (3-d) material circulation driven by waves in the atmosphere was proposed based on recently-derived formulas by Kinoshita and Sato (2013a). The formulas are applicable both to Rossby waves and to gravity waves. Although this theory considered time mean for the averaging of flux calculation, underlying assumption for the formulation is that the temporal and/or spatial scales of the mean (more precisely speaking, background) field are much longer than those of the perturbation field. Thus the formulas can be applied also to stationary waves. The 3-d residual mean flow is divided into three components, i.e., balanced mean flow, unbalanced mean flow and Stokes drift. The last two components are induced by wave forcing, and the sum of their zonal mean is equivalent to the 2-d residual mean flow in the TEM system. It was shown that the unbalanced mean flow is estimated by the momentum flux divergence, while the Stokes drift is directly calculated by the divergence of heat flux and $\overline{S_{(p)}}$. Moreover, by taking it into account that the averaging is inherently needed to remove an oscillatory component of unaveraged quadratic function on a scale of one-half the wavelength of the wave field, we proposed the utilization of an extended Hilbert transform. This extended Hilbert transform was newly introduced in the present paper. Here, the whole scale of the wave packet corresponds to the scale of the "mean" field which the wave packet interacts with.

By applying this method to the outputs from simulation by a gravity-wave resolving general circulation model, the 3-d structure of the residual mean circulation in the middle and upper stratosphere and mesosphere was examined for January and July. Characteristics of the residual mean flow in January and July were roughly a mirror image of each other. An important result was that the residual mean circulation is not zonally uniform in any altitude region.

In the middle and upper stratosphere, the zonal mean meridional component of the residual mean circulation was from the subtropical region of the summer hemisphere to the high latitudes of the winter hemisphere. This meridional flow was divided into three parts according to the dominant terms of the wave activity flux convergence: poleward Stokes drift by PW in the winter hemisphere high latitudes which was largely canceled by equatorward unbalanced mean flow due to PW, poleward unbalanced mean flow by PW in middle and low latitudes of the winter hemisphere, and equatorward unbalanced mean flow by GW in the summer hemisphere. In the winter hemisphere high latitudes, the poleward Stokes drift and equatorward unbalanced mean flow were large in different longitude regions. Thus, even in the winter hemisphere, there were some longitude regions where equatorward flow was dominant. In the summer hemisphere, the unbalanced mean flow was strong in and slightly to the east of the monsoon region. This is likely because the monsoon convection is a dominant source of GW propagating eastward.

In the mesosphere, GW were the most important wave to drive the residual mean circulation. In addition, the contribution of PW generated by baroclinic/barotropic instability was not negligible in the winter hemisphere. The distribution of the residual mean flow is not zonally uniform, which is likely due to nonzonal GW source distribution in both winter and summer hemispheres, to the filtering of GW in the polar night jet largely disturbed by PW in the winter stratosphere, and to the characteristics of the instability in the winter mesosphere. There was some similarity in the structure of the vertical component of the residual mean flow between the stratosphere and mesosphere. This resemblance was roughly understood by the downward control principle.

The atmosphere is coupled vertically by various-kinds of waves with various scales originating from nonzonal sources and propagating three dimensionally. It is considered that the 3-d analysis proposed by the present study must improve our understanding of the vertical coupling processes including wave-wave interaction as well as wave-mean flow interaction. Moreover, it is interesting to examine barotropic/baroclinic instability in terms of the three dimensional structure.

Application of the extended Hilbert transform to obtain eddy and flux quadratics as shown by the present study is available also for the other equation systems such as the quasi-geostrophic system. The use of this method is effective to estimate fluxes and variances associated with wave packets, because the phase interferences among multiple sinusoidal waves are properly included. This point is an advantage compared with the other formulas of 3-d wave activity flux proposed by previous studies which inherently assume a monochromatic wave.

Acknowledgments.

This study is supported by Grant-in-Aid for Scientific Research (A) 25247075 of the Ministry of Education, Culture, Sports and Technology (MEXT), Japan. The authors thank Theodore G. Shepherd and Alan Plumb for constructive comments. Thanks are also due to Yuki Yasuda for his providing schematic figure to illustrate the extended Hilbert transform and useful discussion on the theoretical aspect of the present study. The model simulation was conducted using the Earth Simulator by the KANTO project members. A part of the simulation was made as a contribution to the Innovative Program of Climate Change Projection for the 21st Century supported by MEXT.

REFERENCES

Andrews, D. G., J. R. Holton, and C. B. Leovy, 1987: *Middle Atmosphere Dynamics*. Academic Press, 489pp pp.

Andrews, D. G. and M. E. McIntyre, 1976: Planetary waves in horizontal and vertical shear: The generalized eliassen-palm relation and the mean zonal acceleration. *J. Atmos. Sci.*, **33**, 2031–2048.

Birner, T. and H. Bönisch, 2011: Residual circulation trajectories and transit times into the extratropical lowermost stratosphere. *Atmos. Chem. Phys.*, **11**, 817–827, doi:10.5194/acp-11-817-2011.

Bracewell, R., 1999: *The Fourier Transform and Its Applications*. McGraw-Hill Science/Engineering/Math, 640pp pp.

Butchart, N., et al., 2006: Simulations of anthropogenic change in the strength of the Brewer?Dobson circulation. *Clim. Dyn.*, 727–741, doi:10.1007/s00382-006-0162-4.

Butchart, N., et al., 2010: Chemistry-climate model simulations of twenty-first century stratospheric century stratospheric. *J. Climate*, 5349–5374, doi:10.1175/2010JCLI3404.1.

Callaghan, P. F. and M. L. Salby, 2002: Three-dimensionality and forcing of the Brewer?Dobson circulation. *J. Atmos. Sci.*, **59**, 976–991.

Calvo, N. and R. R. Garcia, 2009: Wave forcing of the tropical upwelling in the lower stratosphere under increasing concentrations of greenhouse gases. *J. Atmos. Sci.*, **66**, 3184–3196.

Dunkerton, T. J., C.-P. F. Hsu, and M. E. McIntyre, 1981: Some eulerian and lagrangian diagnostics for a model stratospheric warming. *J. Atmos. Sci.*, **38**, 819–843.

Dunkerton, T. J., 1978: On the mean meridonal mass motions of the stratosphere and mesosphere. *J. Atmos. Sci.*, **35**, 2325–2333.

Garcia, R. R. and W. J. Randel, 2008: Acceleration of the Brewer-Dobson circulation due to increases in greenhouse gases. *J. Atmos. Sci.*, **65**, 2731–2739, doi:10.1175/2008JAS2710.1.

Haynes, P. H., M. E. McIntyre, T. G. Shepherd, C. J. Marks, and K. P. Shin, 1991: On the "Downward Control" of extratropical diabatic circulations by eddy-induced mean zonal forces. *J. Atmos. Sci.*, **48**, 651–678.

Hitchman, M. H. and M. J. Rogal, 2010: Influence of tropical convection on the southern hemisphere ozone maximum during the winter to spring transition. *J. Geophys. Res.*, **115**, 8325, doi:10.1029/2001JD001034.

Holton, J. R., P. H. Haynes, M. E. McIntyre, A. R. Douglass, R. B. Rood, and L. Pfister, 1995: Stratosphere-troposphere exchange. *Rev. Geophys.*, **33**, 403–439.

Holton, J. R., 1982: The role of gravity wave induced drag and diffusion in the momentum budget of the mesosphere. *J. Atmos. Sci.*, **39**, 791–799.

Kawatani, Y. and K. Hamilton, 2011: The quasi-biennial oscillation in a double CO2 climate. *J. Atmos. Sci.*, **68**, 265–283, doi:10.1175/JAS3953.1.

Kawatani, Y., K. Sato, T. J. Dunkerton, S. Watanabe, S. Miyahara, and M. Takahashi, 2010: The roles of equatorial trapped waves and internal inertia-gravity waves in driving the quasi-biennial oscillation. Part I: Zonal mean wave forcing. *J. Atmos. Sci.*, 963–980.

Kinoshita, T. and K. Sato, 2013a: A formulation of three-dimensional residual mean flow applicable both to inertia-gravity waves and to rossby waves. *J. Atmos. Sci.*, 1577–1602.

Kinoshita, T. and K. Sato, 2013b: A formulation of unified three-dimensional wave activity flux of inertia-gravity waves and rossby waves. *J. Atmos. Sci.*, 1603–1615.

Lieberman, R. S., 1999: The gradient wind in the mesosphere and lower thermosphere. *Earth Planets Space*, 751–761.

Lindzen, R. S., 1981: Turbulence and stress owing to gravity wave and tidal breakdown. *J. Geophys. Res.*, **86**, 9707–9714.

Lin, P., Q. Fu, S. Solomon, and J. M. Wallace, 2009: Temperature trend patterns in southern hemisphere high latitudes: Novel indicators of stratospheric change. *J. Climate*, **22**, 6325–6341.

Li, F., J. Austin, and J. Wilson, 2008: The strength of the Brewer-Dobson circulation in a changing climate: A coupled chemistry-climate model simulation. *J. Climate*, **21**, 40–57.

Li, F., R. S. Stolarski, S. Pawson, P. A. Newman, and D. Waugh, 2010: Narrowing of the upwelling branch of the Brewer]Dobson circulation and Hadley cell in chemistry]climate model simulations of the 21st century. *Geophys. Res. Lett.*, **37**, L12114, doi:10.1029/2004GL019562.

Matsuno, T., 1982: A quasi one-dimensional model of the middle atmosphere circulation interacting with internal gravity waves. *J. Meteorol. Soc. Japan*, 215–226.

McLandress, C. and T. G. Shepherd, 2009: Simulated anthropogenic changes in the Brewer-Dobson circulation, including its extension to high latitudes. *J. Climate*, **22**, 1516–1540, doi:10.1175/2008JCLI2679.1.

Miyahara, S., D. Yamamoto, and Y. Miyoshi, 2000: On the geostrophic balance of mean zonal winds in the mesosphere and lower thermosphere. *J. Meteorol. Soc. Jpn*, **78**, 683–688.

Miyazaki, K., S. Watanabe, Y. Kawatani, Y. Tomikawa, M. Takahashi, and K. Sato, 2010: Transport and mixing in the extratropical tropopause region in a high vertical resolution GCM. Part I: Potential vorticity and heat budget analysis. *J. Atmos. Sci.*, 1293–1314.

Norton, W. A., 2006: Tropical wave driving of the annual cycle in tropical tropopause temperatures. part ii: Model results. *J. Atmos. Sci.*, **63**, 1420–1431.

Okamoto, K., K. Sato, and H. Akiyoshi, 2011: A study on the formation and trend of the brewer-dobson circulation. *J. Geophys. Res.*, **116**, doi:10.1029/2010JD014953.

Plumb, R. A., 2002: Stratospheric transport. *J. Meteorol. Soc. Jpn*, **80**, 793–809.

Preusse, P., A. Dörnbrack, S. D. Eckermann, M. Riese, B. Schaeler, J. T. Bacmeister, D. Broutman, and K. U. Grossmann, 2002: Space-based measurements of stratospheric mountain waves by CRISTA, 1. Sensitivity, analysis method, and a case study. *J. Geophys. Res.*, **107**, 8178, doi:10.1029/2001JD000699.

Randel, W. J., M. Park, L. Emmons, D. Kinnison, P. Bernath, K. A. Walker, C. Boone, and H. Pumphrey, 2010: Asian monsoon transport of pollution to the stratosphere. *Science*, **328**, 611–613.

Randel, W. J., 1987: The evaluation of winds from geopotential height data in the stratosphere. *J. Atmos. Sci.*, **44**, 3097–3120.

Rosenlof, K. H., 1995: Seasonal cycle of the residual mean meridional circulation in the stratosphere. *J. Geophys. Res.*, **100**, 5173–5191.

Sato, K., D. O'Sullivan, and T. J. Dunkerton, 1997: Low-frequency inertia-gravity waves in the stratosphere revealed by three-week continuous observation with the mu radar. *Geophys. Res. Lett.*, **24**, 1739–1742.

Sato, K., S. Tateno, S. Watanabe, and Y. Kawatani, 2012: Gravity wave characteristics in the southern hemisphere revealed by a high-resolution middle-atmosphere general circulation model. *J. Atmos. Sci.*, **69**, 1378–1396, doi:http://dx.doi.org/10.1175/JAS-D-11-0101.1.

Sato, K., Y. Tomikawa, G. Hashida, T. Yamanouchi, H. Nakajima, and T. Sugita, 2009a: Longitudinal dependence of ozone recovery in the Antarctic polar vortex revealed by balloon and satellite observations. *J. Atmos. Sci.*, **66**, 1807–1820.

Sato, K., S. Watanabe, Y. Kawatani, Y. Tomikawa, K. Miyazaki, and M. Takahashi, 2009b: On the origins of mesospheric gravity waves. *Geophys. Res. Lett.*, **36**, L19801, doi:10.1029/2009GL039908.

Sato, K., M. Yamamori, S. Ogino, N. Takahashi, Y. Tomikawa, and T. Yamaouchi, 2003: A meridional scan of the stratospheric gravity wave field over the ocean in 2001 (MeSSO2001). *J. Geophys. Res.*, **108**, 4491, doi:10.1029/2002JD003219.

Seidel, D. J. and W. J. Randel, 2007: Recent widening of the tropical belt: Evidence from tropopause observations. *J. Geophys. Res.*, **112**, D20 113.

Seviour, W. J. M., N. Butchart, and S. C. Hardiman, 2012: The Brewer?Dobson circulation inferred from ERA-Interim. *Q. J. Roy. Met. Soc.*, **138**, 878–888.

Shepherd, T. G. and C. McLandress, 2011: Strengthening of the Brewer-Dobson circulation in response to climate change:critical-layer control of subtropical wave breaking. *J. Atmos. Sci.*, **68**, 784–797.

Smith, A. K., 2003: The origin of stationary planetary waves in the upper mesosphere. *J. Atmos. Sci.*, **60**, 3033–3041.

Ueyama, R. and J. M. Wallace, 2010: To what extent does high-latitude wave forcing drive tropical upwelling in the Brewer-Dobson circulation? *J. Atmos. Sci.*, **67**, 1232–1246.

Watanabe, S., Y. Kawatani, Y. Tomikawa, K. Miyazaki, M. Takahashi, and K. Sato, 2008: General aspects of a T213L256 middle atmosphere general circulation model. *J. Geophys. Res.*, **113**, D12110, doi:10.1029/2008JD010026.

Watanabe, S., Y. Tomikawa, K. Sato, Y. Kawatani, K. Miyazaki, and M. Takahashi, 2009: Simulation of the eastward 4-day wave in the Antarctic winter mesosphere using a gravity wave resolving general circulation model. *J. Geophys. Res.*, **114**, D16111, doi:10.1029/2008JD011636.

List of Figures

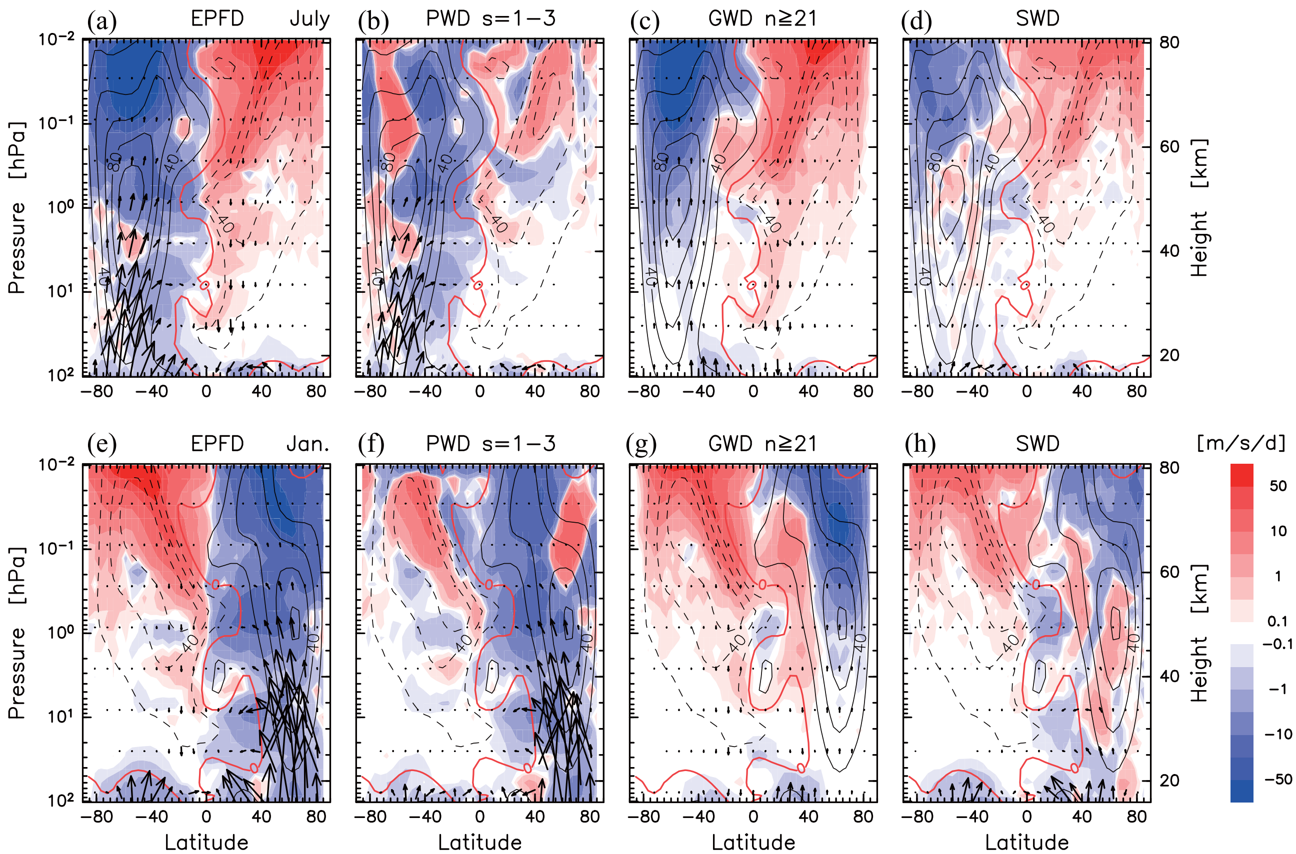

FIG. 1. Meridional cross sections of E-P flux vector and its divergence (colors) for (a) all resolved waves (EPFD), (b) planetary waves (PWD), (c) gravity waves (GWD), and (d) synoptic-scale waves (SWD) averaged in July of the 2nd year, and (e)–(h) are those in January of the 2nd year. Contours of zonal mean zonal winds are superimposed on all panels. Contour intervals are every 20 ms^{-1}. Broken contours show negative values.

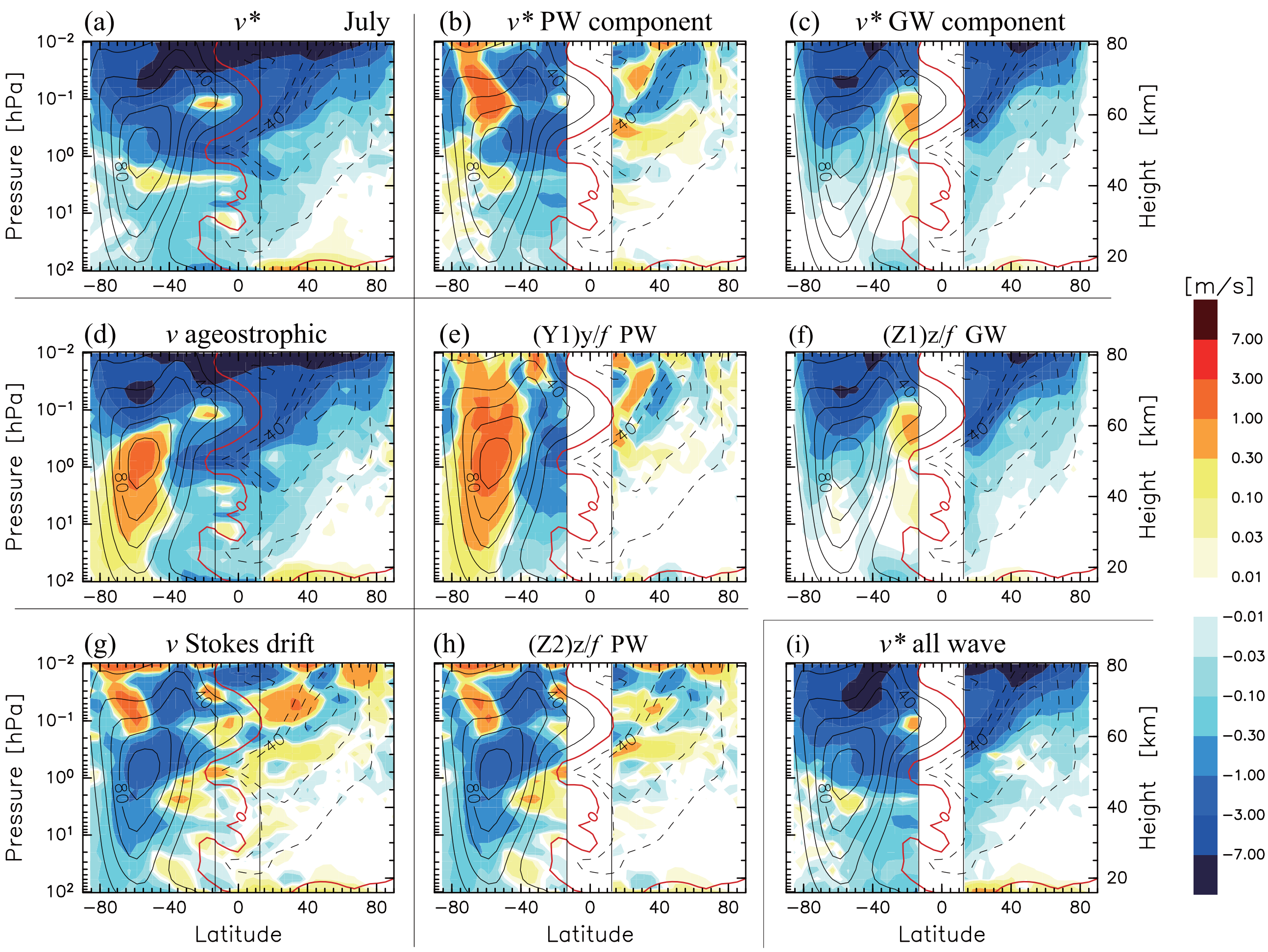

FIG. 2. Meridional cross sections of (a) the meridional component of the residual mean flow ($[v]^*$), (b) and (c) contributions of PW and GW that are estimated using the downward control principle (DCP), respectively, (d) zonal mean meridional velocity ($[v]_{\mathrm{a}}$), (e) its contribution by PW ($Y_{1y}/\hat{f}$) and (f) by GW ($Z_{1z}/\hat{f}$), (g) meridional component of the Stokes drift ($[v]^{\mathrm{S}}$), (h) its contribution by PW, and (i) $[v]^*$ estimated using EPFD due to all waves by DCP that are averaged in July. Contours show zonal mean zonal winds with an interval of 20 ms^{-1}.

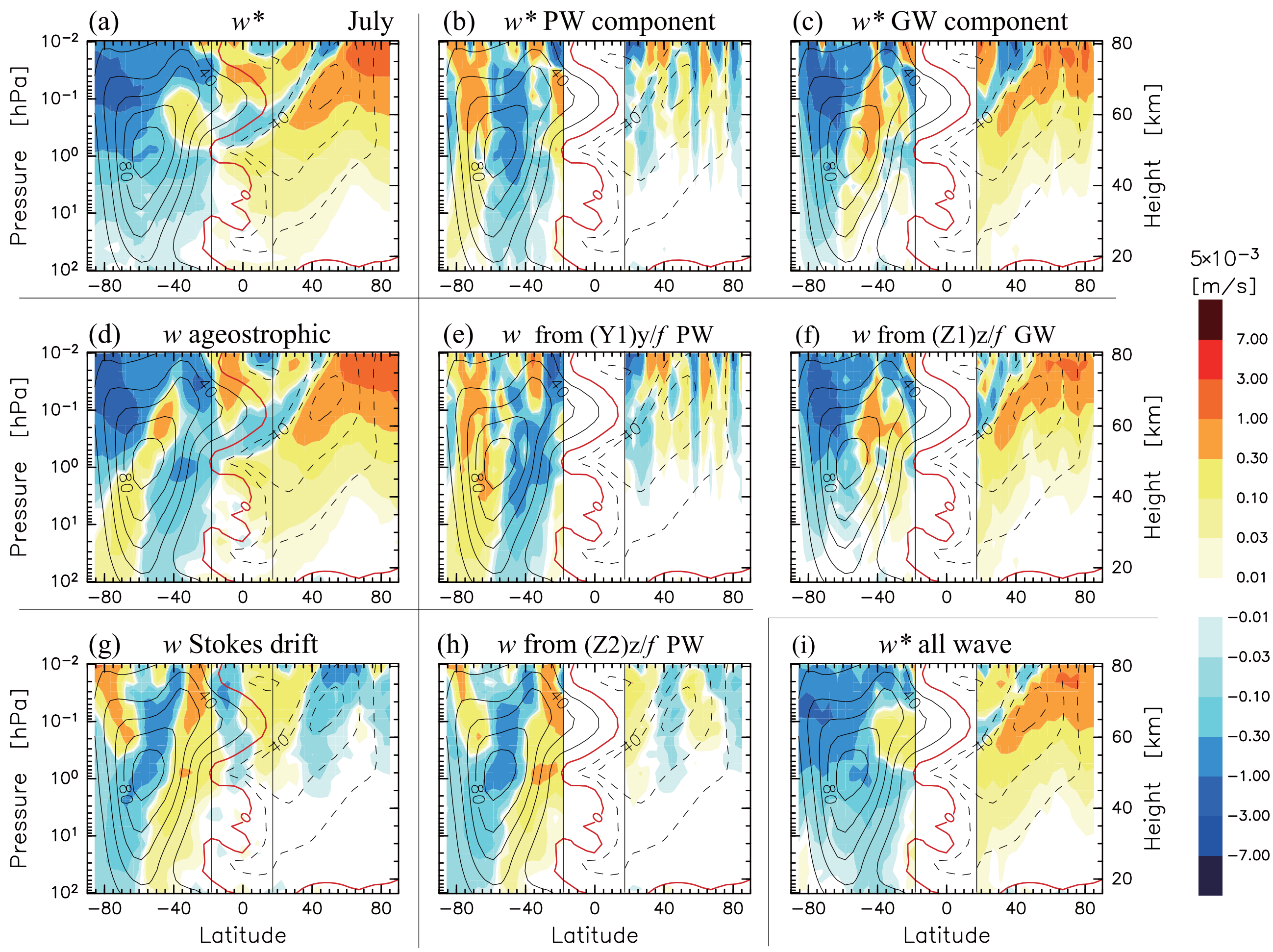

FIG. 3. The same as Fig. 2 but for the vertical component.

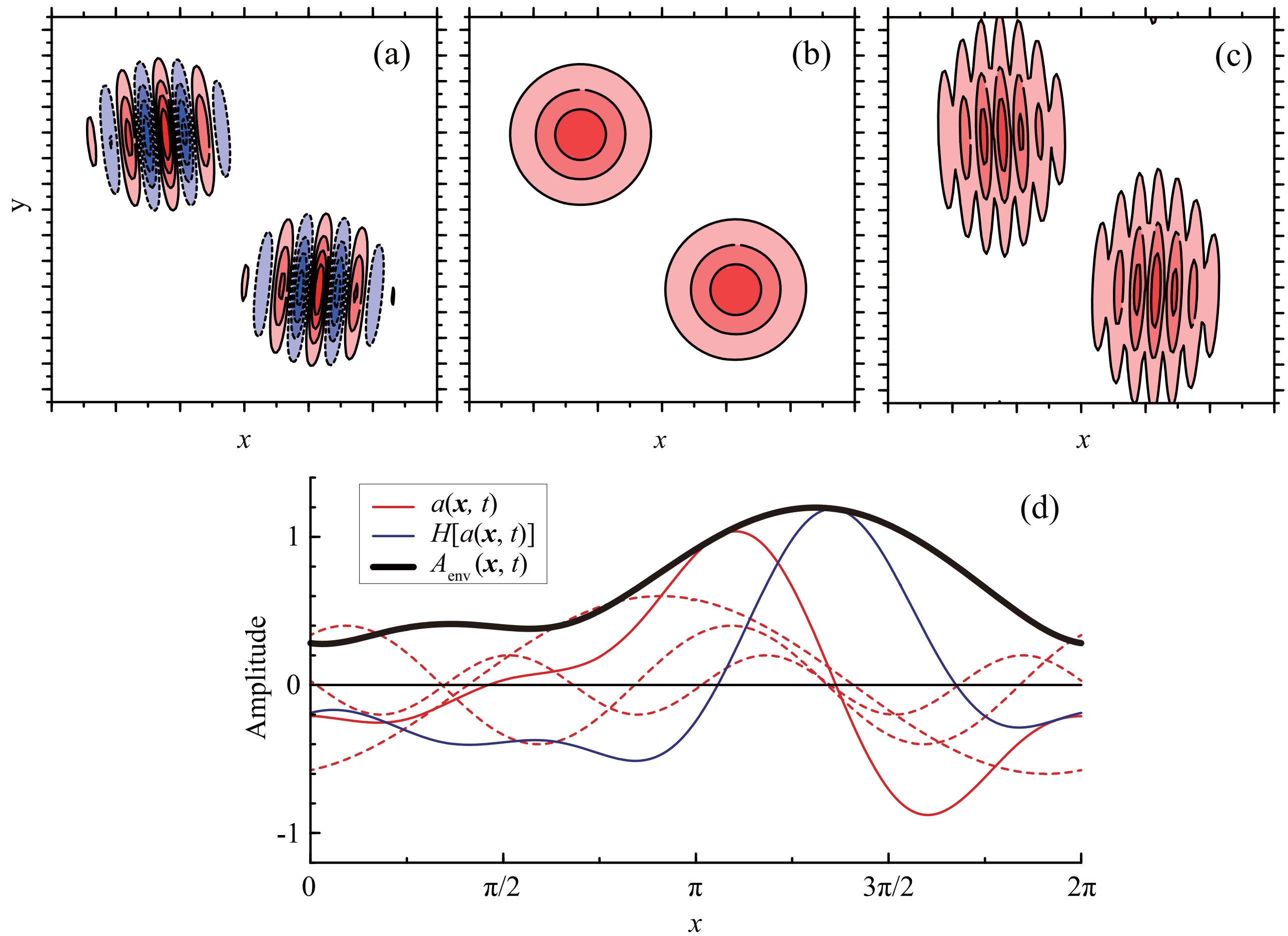

FIG. 4. An illustration of the estimation method of envelop function using the extended Hilbert transform (e-HT). (a) The fluctuation field forming two wave packets. (b) and (c) Estimates of the envelop function using e-HT in the x and y directions, respectively. (d) Application of the e-HT to stationary waves. The sold red curve shows a longitudinal (x) profile of a particular quantity $a(x,t)$ that is composed of $s = 1, 2, 3$ wave components (red dashed curves). The e-HT of $a(x,t)$ $(H[a(x,t)])$ in the x direction is shown by the blue curve. The envelop function $A_{\rm env}(x,t)$ is shown in the black curve.

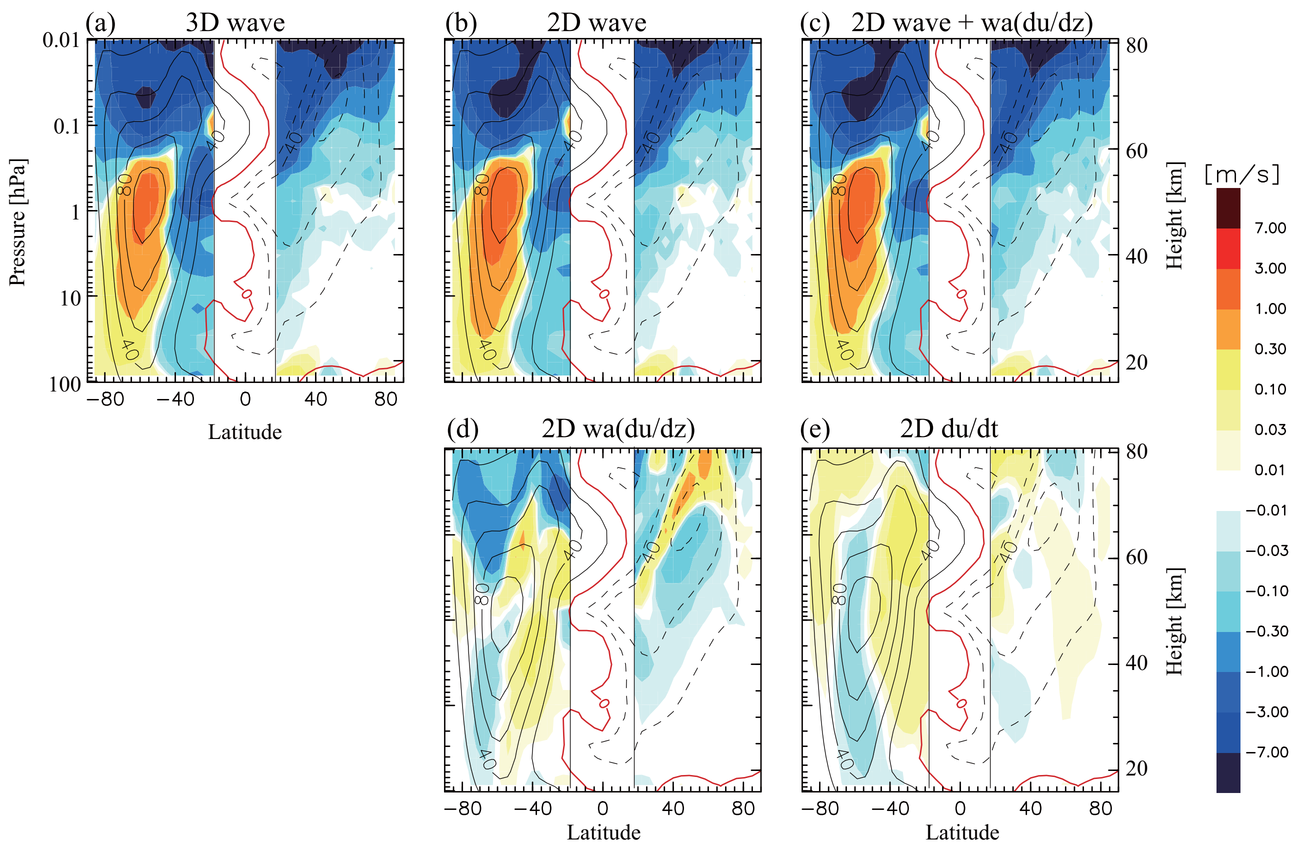

FIG. 5. Meridional cross sections of zonal mean unbalanced mean meridional flow calculated (a) from 3-d momentum flux divergence ($\overline{v}_{\mathrm{a}}$) and (b) from 2-d momentum flux divergence $[v]_{\mathrm{a}}$, and (c) from 2-d momentum flux divergence plus vertical advection of zonal mean zonal wind, (d) vertical advection of zonal mean wind, and (e) tendency of zonal mean zonal wind in July of the 2nd year. Contours show zonal mean zonal winds with an interval of 20 ms^{-1}.

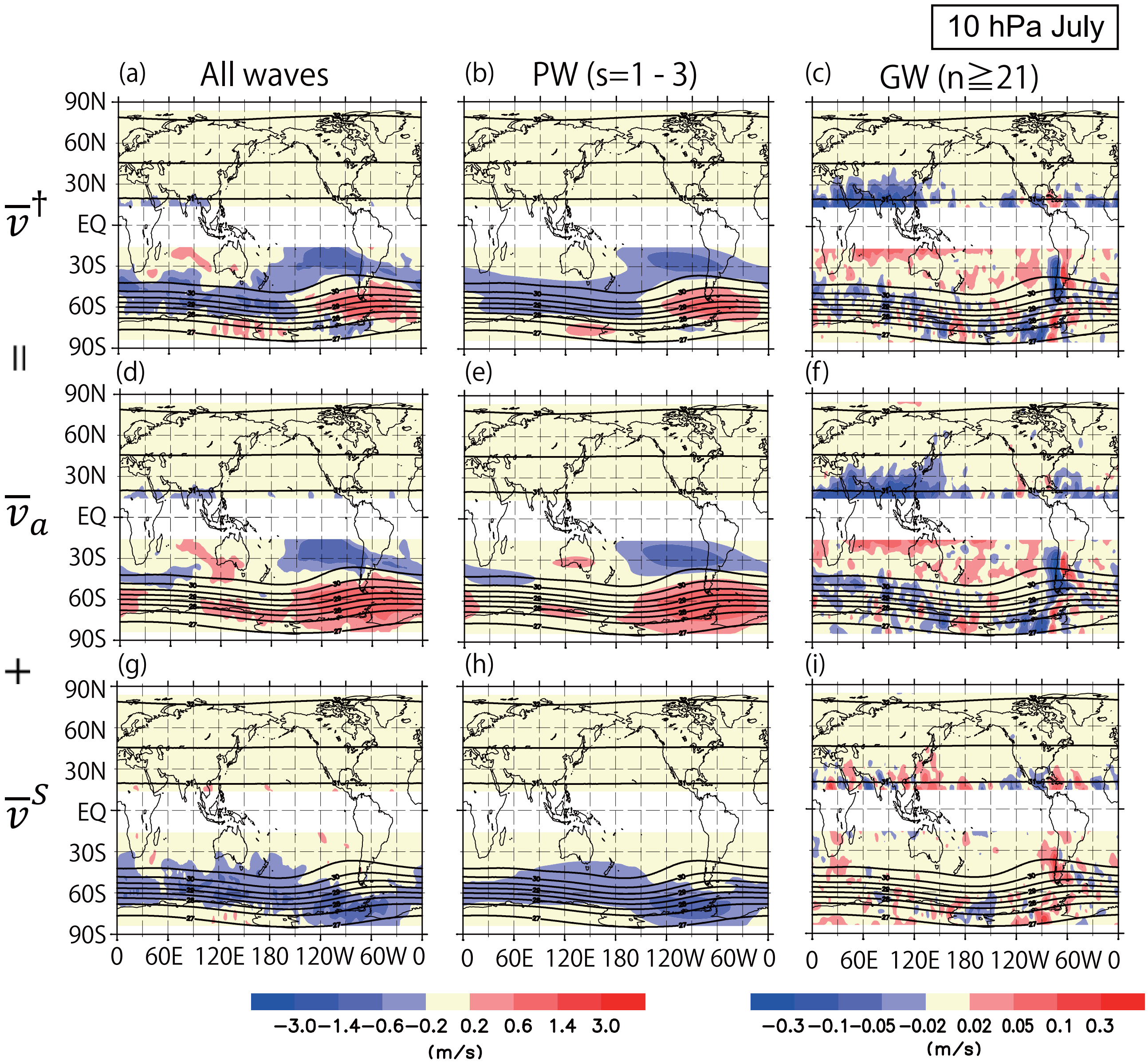

FIG. 6. Horizontal maps of (top) 3-d residual mean flow $\overline{v}^{\dagger}$, (middle) unbalanced mean flow $\overline{v}_{\mathrm{a}}$, and (bottom) Stokes drift $\overline{v}^{\mathrm{S}}$ due to (left) all waves, (middle) PW, and (right) GW at 10 hPa in July of the 2nd year by colors. Contours show monthly-mean geopotential heights with an interval of 0.5×10^{3} m. Note that color scales are different between the figures of all waves and PW and those for GW.

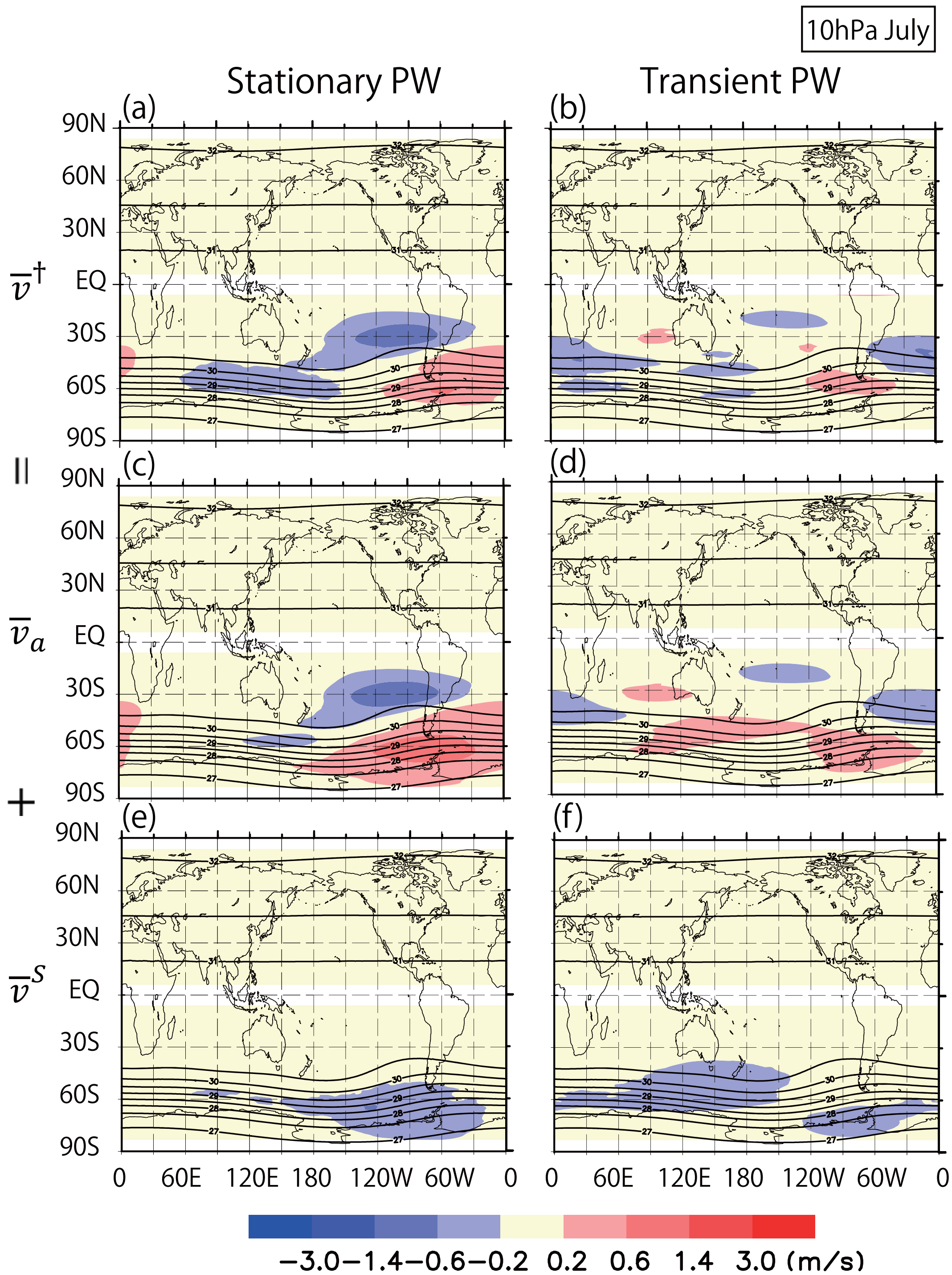

FIG. 7. The same as Fig. 6 but for (left) stationary PW and (right) transient PW.

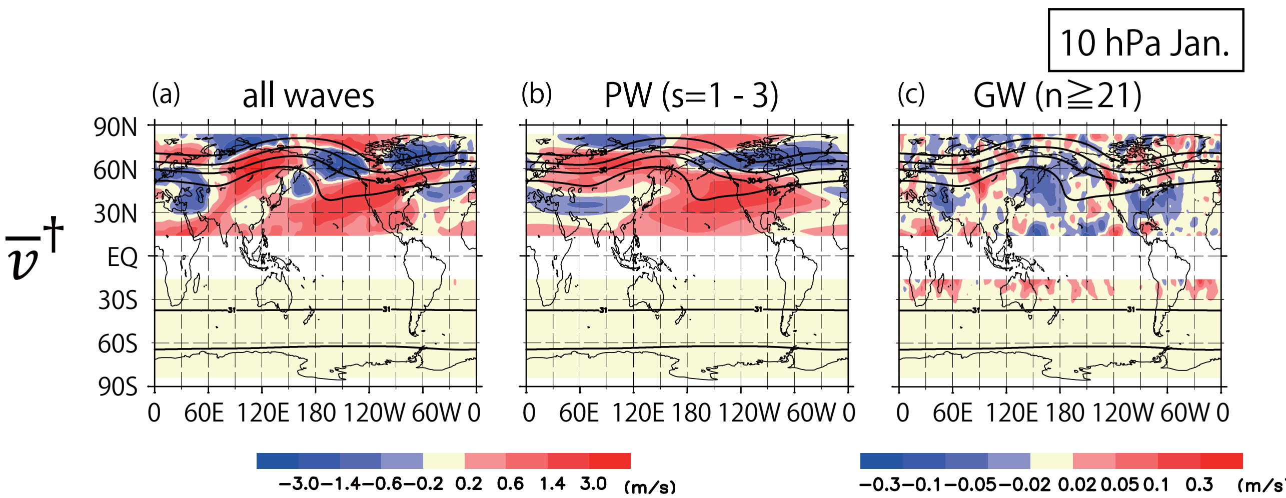

FIG. 8. The same as Fig. 6 but for (a) 3-d residual mean flow $\overline{v}^{\dagger}$, and (b) and (c) contributions by PW and by GW, respectively, at 10 hPa in January of the 2nd year.

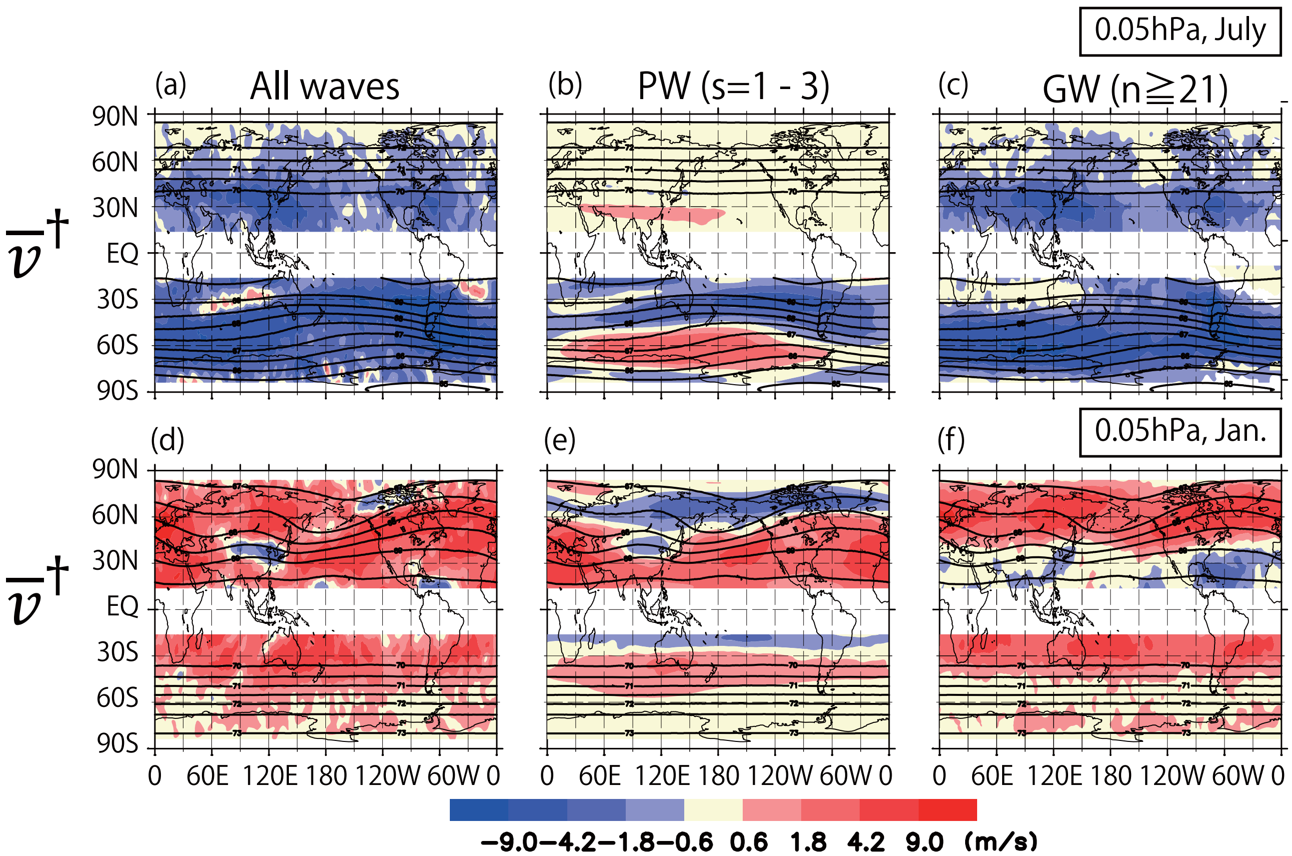

FIG. 9. The same as Fig. 6 but for (a) 3-d residual mean flow $\overline{v}^\dagger$, and (b) and (c) contributions by PW and by GW, respectively, at 0.05 hPa in July of the 2nd year, and (d) (e) and (f) are those in January of the 2nd year. Color scales are taken different from those of Fig. 6.

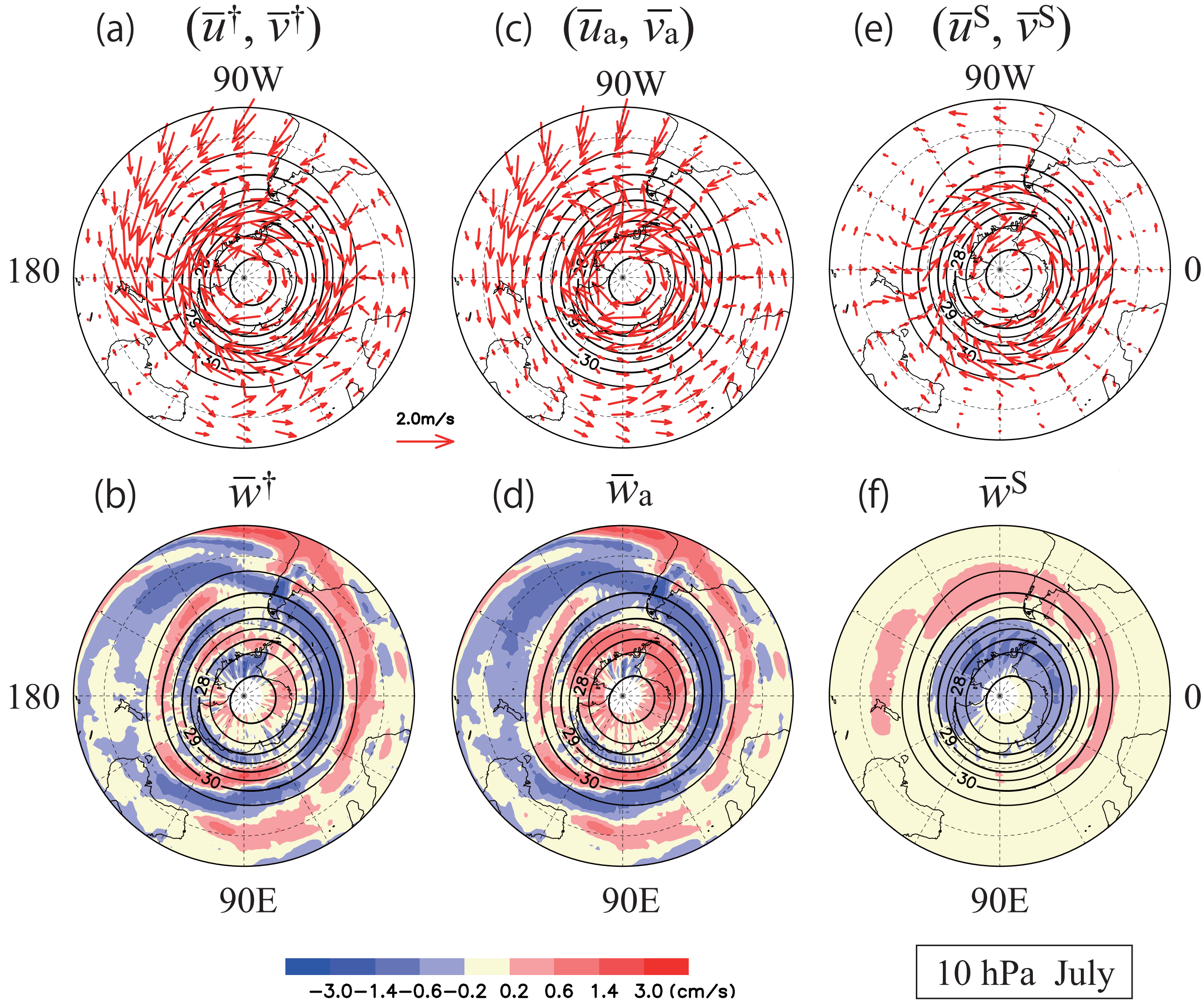

FIG. 10. Polar stereographic projection maps of (left) the residual mean flow induced by waves, (middle) unbalanced mean flow, and (right) Stokes drift at 10 hPa in SH in July of the 2nd year. Top panels show their horizontal component vectors by arrows, and bottom panels show their vertical component by colors. Contours show monthly-mean geopotential heights with an interval of 0.5×10^3 m.

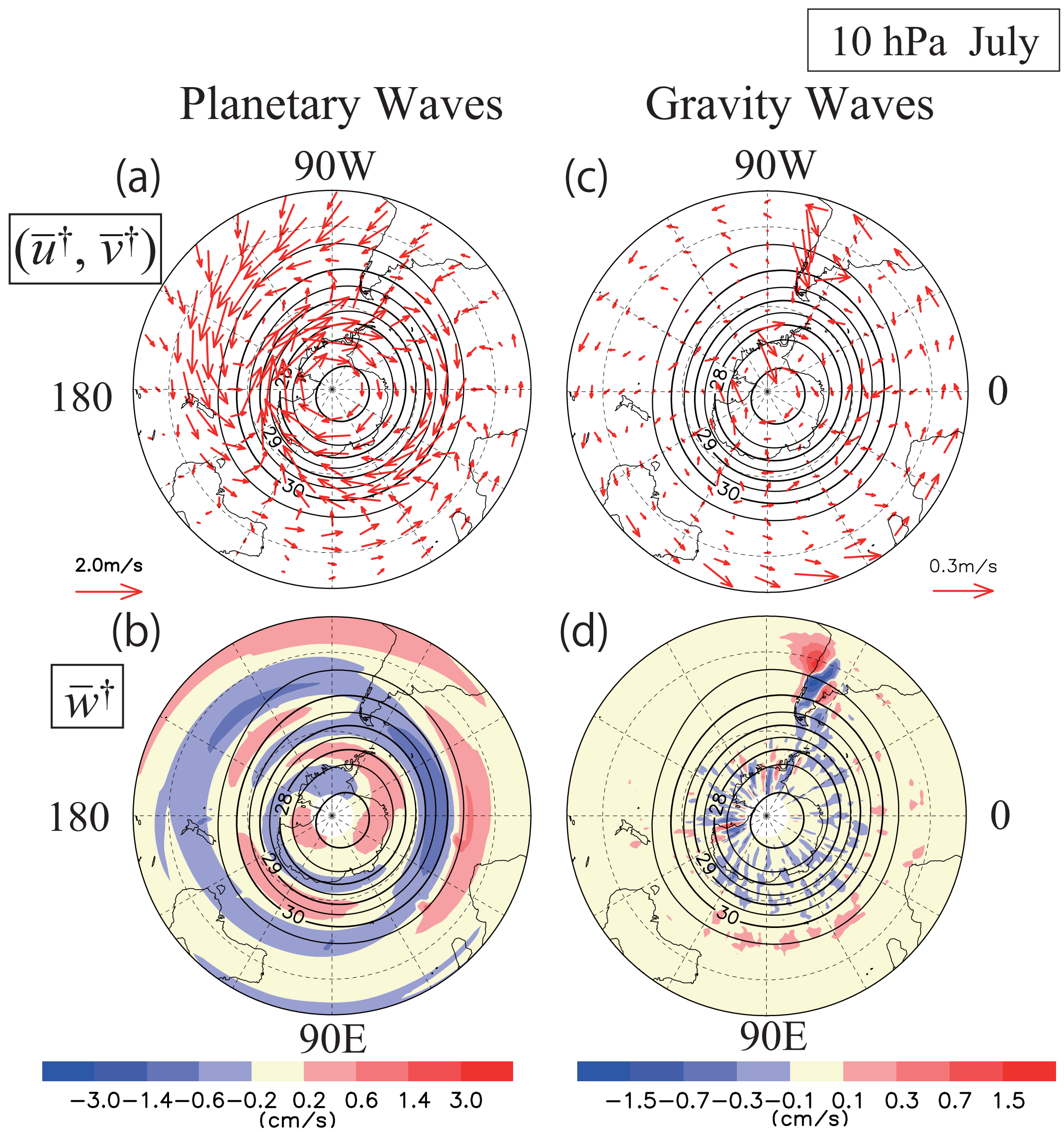

FIG. 11. Polar stereographic projection maps of the residual mean flow induced (left) by PW and (right) by GW in SH. Top panels show their horizontal component vectors by arrows, and bottom panels show their vertical component by colors. Contours show monthly-mean geopotential heights with an interval of 0.5×10^3 m. Note that unit vectors for (a) and (c) are different.

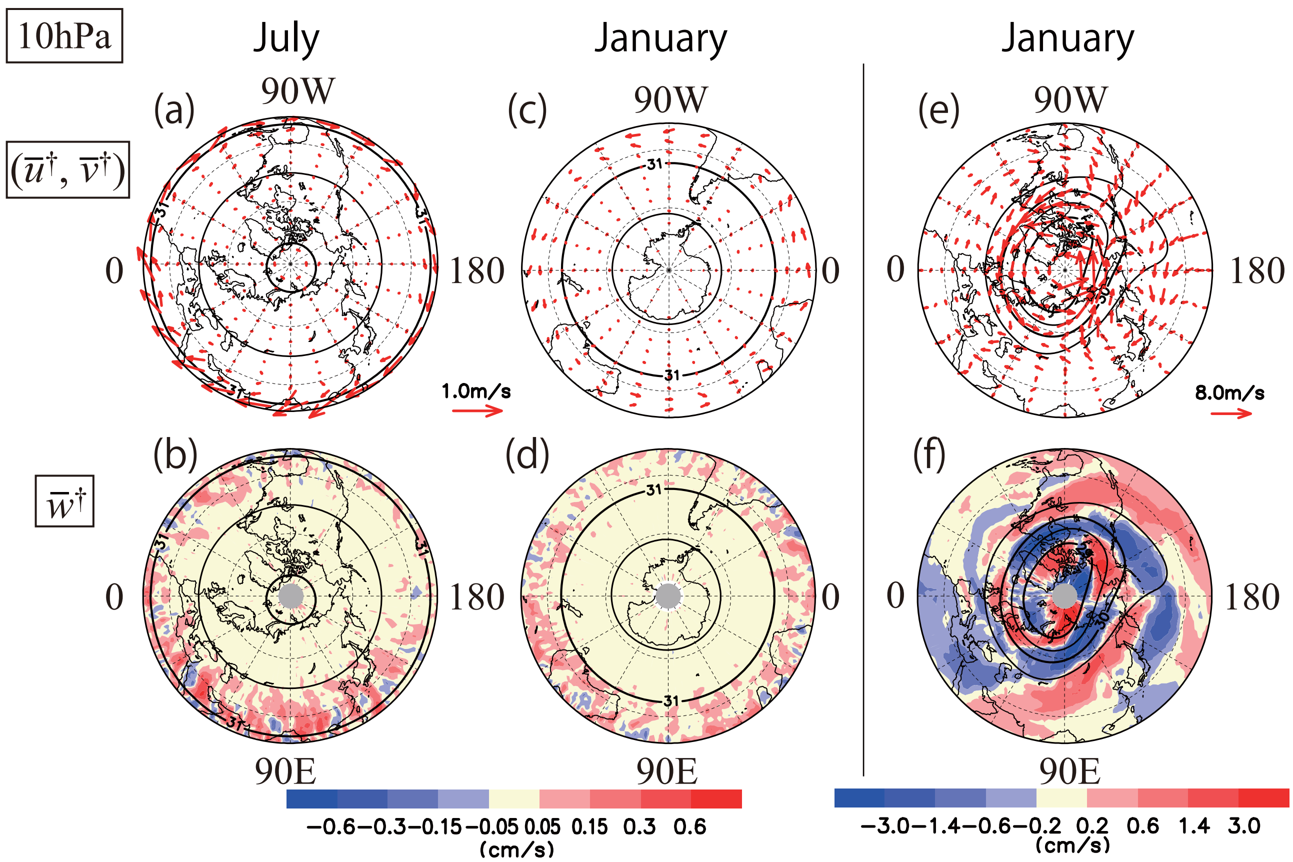

FIG. 12. The same as Figs. 10a and 10b but (a) and (b) for NH in July of the 2nd year, (c) and (d) ((e) and (f)) for SH (NH) in January of the 2nd year. Note that color scales and unit vectors are different between the summer and winter hemispheres.

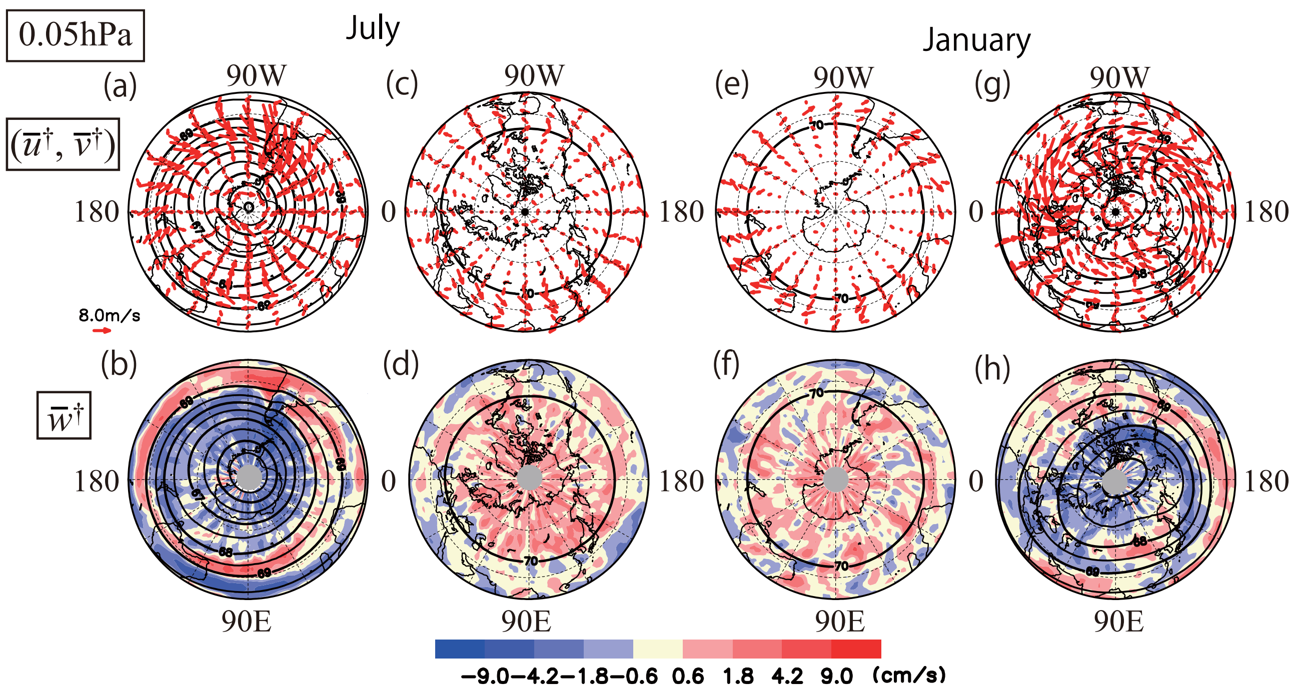

FIG. 13. The same as Figs. 10a and 10b but for 0.05 hPa in respective months and respective hemispheres in the mesosphere.

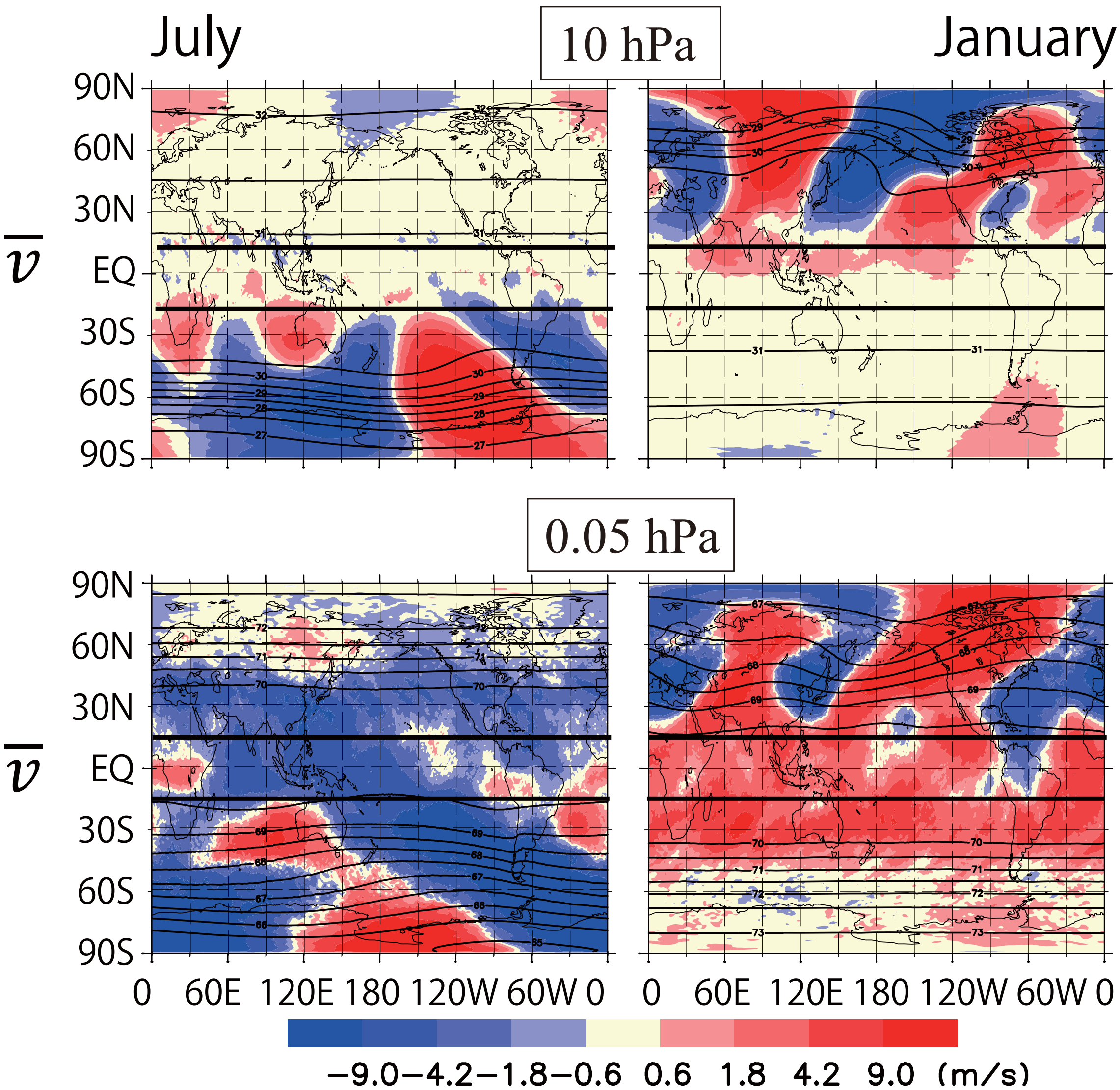

FIG. 14. Horizontal maps of monthly mean meridional wind $\overline{v}$ at 10 hPa (top) and 0.05 hPa (bottom) in July (left) and January (right). Note that color scales for 10 hPa are different from those for Fig. 10.